BGAE: Auto-Encoding Multi-View Bipartite Graph Clustering

Liang Li, Yuangang Pan, Jie Liu, Yue Liu, Xinwang Liu, *Senior Member, IEEE*, Kenli Li, *Senior Member, IEEE*, Ivor W. Tsang, *Fellow, IEEE*, and Keqin Li, *Fellow, IEEE*

***Abstract*—Unsupervised multi-view bipartite graph clustering (MVBGC) is a fast-growing research, due to promising scalability in large-scale tasks. Although many variants are proposed by various strategies, a common design is to construct the bipartite graph directly from the input data, i.e., only consider the unidirectional "encoding" process. However, "encoding-decoding" mechanism is a popular design for deep learning, the most representative one is auto-encoder (AE). Enlightened by this, this paper rethinks existing MVBGC paradigms and transfers the "encoding-decoding" design into graph machine learning, and proposes a novel framework termed auto-encoding multi-view bipartite graph clustering (BGAE), which integrates encoding, bipartite graph construction, and decoding modules in a self-supervised learning manner. The encoding module extracts a latent joint representation from the input data, the bipartite graph construction module learns a bipartite graph with connectivity constraint in latent semantic space, and the decoding module recreates the input data via the bipartite graph. Therefore, our novel BGAE combines representation learning, bipartite graph learning, reconstruction learning, and label inference into a unified framework. All the modules are seamlessly integrated and mutually reinforcing for clustering-friendly purposes. Extensive experiments verify the superiority of our novel design and the significance of "decoding" process. To the best of our knowledge, this is the first attempt to explore "encoding-decoding" design in traditional MVBGC.**

***Index Terms*—Bipartite graph learning, encoding-decoding, graph machine learning, multi-view clustering.**

Manuscript received 7 July 2023; revised 2 December 2023; accepted 30 January 2024. Date of publication 7 February 2024; date of current version 12 July 2024. This work was supported in part by the National Science Fund for Distinguished Young Scholars of China under Grant 62325604, in part by the National Key Research and Development Program of China under Grant 2021YFB0300101, in part by the National Natural Science Foundation of China under Grant 62276271, in part by A*STAR under Grant C22281201, and in part by China Scholarship Council under Grant 202306110001. Recommended for acceptance by W. Zhao. *(Corresponding author: Xinwang Liu.)*

Liang Li, Yue Liu, and Xinwang Liu are with the School of Computer, National University of Defense Technology, Changsha 410073, China (e-mail: liliang1037@gmail.com; yueliu19990731@163.com; xinwangliu@nudt.edu.cn).

Yuangang Pan and Ivor W. Tsang are with the Center for Frontier AI Research, Agency for Science, Technology and Research (A*STAR), Singapore 138632 (e-mail: yuangang.pan@gmail.com; ivor_tsang@cfar.a-star.edu.sg).

Jie Liu is with the Science and Technology and Parallel and Distributed Processing Laboratory, National University of Defense Technology, Changsha 410073, China, and also with the Laboratory of Software Engineering for Complex Systems, National University of Defense Technology, Changsha 410073, China (e-mail: liujie@nudt.edu.cn).

Kenli Li is with the College of Computer Science and Electronic Engineering, Hunan University, Changsha 410073, China, and also with Supercomputing and Cloud Computing Institute, Hunan University, Changsha 410073, China (e-mail: lkl@hnu.edu.cn).

Keqin Li is with the Department of Computer Science, State University of New York, New Paltz, NY 12561 USA (e-mail: lik@newpaltz.edu).

The code is provided at https://github.com/liliangnudt/BGAE.

This article has supplementary downloadable material available at https://doi.org/10.1109/TKDE.2024.3363217, provided by the authors.

Digital Object Identifier 10.1109/TKDE.2024.3363217

I. Introduction

With the rapid growth of data in the real world, human annotations induce expensive costs, developing unsupervised or self-supervised learning is a trend to explore hidden patterns without human intervention [1]. Clustering is a central topic in unsupervised learning to find intrinsic data groupings and latent structures [2]. Owing to the flexibility and powerful capacity of graph to represent complex data structures [3], [4], graph clustering is a fast-growing research [5], [6]. To process multi-view or multimodal data (e.g., image features can be characterized by LBP, PHOG, and GIST) [7], [8], [9], multi-view clustering (MVC) has gained extensive research and achieved superior embeddings or partitions than single-view clustering by fusing consistency and complementarity [10], [11]. Multi-view graph clustering (MVGC) [12], [13] is an active branch, widely applied in data mining, natural language processing, and computer vision [14], [15].

Since traditional MVGC paradigms require building fully connected graphs with cubic time complexity and quadratic space complexity respecting sample number [16], [17], greatly limiting scalability in large-scale applications, multi-view bipartite graph clustering (MVBGC) [18], [19] is developed by building correlations of representative anchors/landmarks and all instances, i.e., bipartite graph. In this way, complexity can be reduced to linear magnitude, greatly expanding scalability.

Many MVBGC models have been proposed by various strategies to construct a "nice" bipartite graph, such as using sampling [20], [21] or optimizing manners [22], [23] to select representative anchors, introducing different regularizations [24] or constraints [25] to refine intrinsic structures, or concatenating multi-scale bipartite graphs [26], [27] across multiple views to achieve ensemble clustering.

By carefully reviewing existing BGC models in graph machine learning, we find that a common design is constructing the bipartite graph directly from the input data, i.e., only focusing on an unidirectional "encoding" process. However, "encoding-decoding" is a prevalent design in deep learning. The most representative model is auto-encoder [28], Fig. 1 shows the sketch. AE is composed of an encoder and a decoder. Encoder plays the role of information extractor to extract discriminative embeddings by multilayer neural networks. The decoder acts as a data reconstructor to recreate the input data from the learned

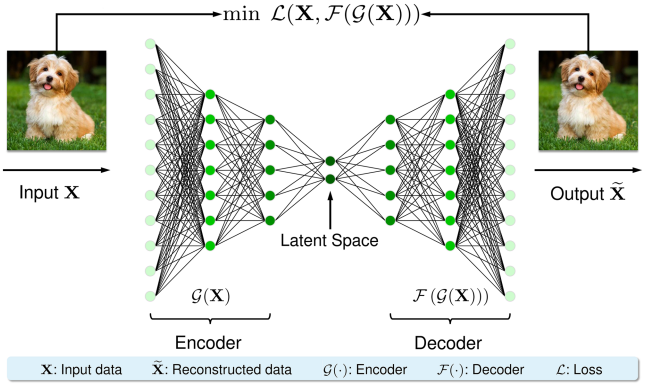

Fig. 1. Sketch of auto-encoder.

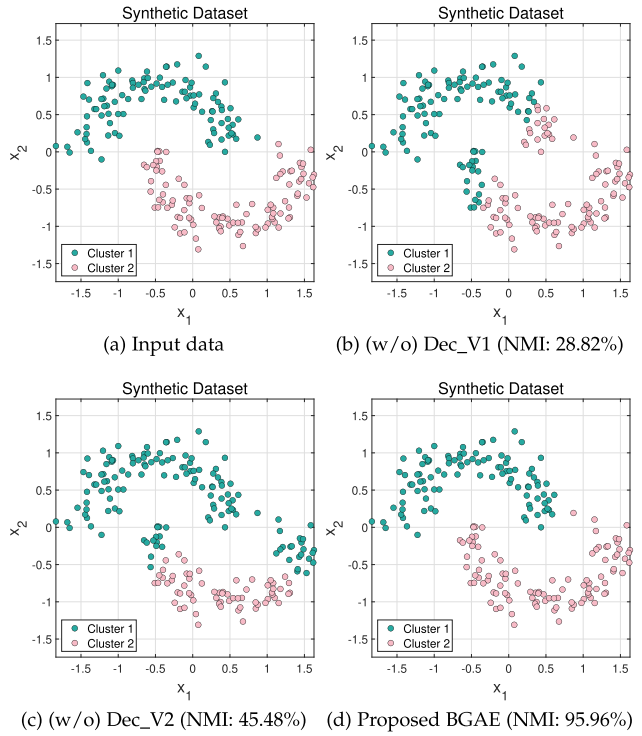

Fig. 2. Visualization of "benefits" from the decoding module on a synthetic dataset. "Decoding" learning provides feedback on optimization, enabling the learned representation not far from input data, thereby retaining the initial manifold. Detailed experimental settings are available in Table V.

intermediate representation. AE has gained great success, and many popular models are derived, such as denoising AE [29], VAE [30], GAE [31], MAE [32], widely applied in dimensionality reduction, image processing, and information retrieval [33]. It has also been extended to multi-view learning and shows promising performance, e.g., it integrates with generative models to fuse consistency and complementarity, serving to predict missing instances. [34].

Enlightened by AE, we transfer the "encoding-decoding" design into traditional graph machine learning and propose a novel "auto-encoding" MVBGC framework, called BGAE. Fig. 3 plots the framework. First, we design an "encoding" module. Considering directly constructing the bipartite graph from input data may be unreliable, as real-world data may involve noise, outliers, or redundancy. Analogously to the encoder, we extract a consistent latent representation across multiple views, and set it to the input of the bipartite graph construction module. Then, we use the graph manifold learning paradigm to learn a bipartite graph, and further enforce it to hold connectivity constraint to output discrete labels directly. Finally, we introduce a "decoding" module. Instead of almost perfectly duplicating the input data from the intermediate representation, we recreate the input data via the bipartite graph. Such a setting not only provides feedback on the learning process, enabling the learned representation not far from the input data to retain the initial manifold, but also accords with the idea of undercomplete AE that avoids "close to perfect" duplication [28]. Fig. 2 visualizes the "benefits" of decoding learning. Compared to the baselines that mistaken partitions with poor performance (NMI: 28.82% and 45.48%), our proposed BGAE well captures the initial manifold with promising performance (NMI: 95.96%).

As a result, our end-to-end "auto-encoding" BGAE integrates representation learning, bipartite graph learning, reconstruction learning, and label inference into a unified framework. The contributions are outlined as follows:

1) Enlightened by the popular AE, we rethinking the traditional MVBGC paradigms in graph machine learning, and find that existing models adopt a common design that constructs the bipartite graph directly from the input data, that is, only consider an unidirectional "encoding" process, but lack the corresponding "decoding" learning.
2) We take the first step towards transferring the "encoding-decoding" design into graph machine learning and propose a novel "auto-encoding" MVBGC model, termed BGAE, integrating representation learning, bipartite graph learning, reconstruction learning, and label inference into a unified framework. All modules are mutually promoted and seamlessly integrated.
3) We design an efficient ADMM solver with linear complexity respecting instances, making it can scale to large-scale tasks. Extensive experiments empirically verify the superiority of our novel design and the significance of the "decoding" process.

II. Related Work

This section briefly reviews related work. Table I collects the main notations.

A. Non-Negative Matrix Factorization

Given the input data $\mathbf{X} \in \mathbb{R}^{\widetilde{d} \times n}$ drawn from k clusters, matrix factorization methods [35], [36] can decompose it into a base matrix $\mathbf{U}$ and a coefficient matrix $\mathbf{V}$. The most representative method is non-negative matrix factorization (NMF) [37] that holds both $\mathbf{U}$ and $\mathbf{V}$ to be non-negative, i.e.,

$$\min_{\mathbf{U},\mathbf{V}} \widetilde{\mathcal{L}}(\mathbf{X}, \mathbf{U}\mathbf{V}), \text{ s.t. } \mathbf{U} \geq 0, \mathbf{V} \geq 0, \tag{1}$$

where $\widetilde{\mathcal{L}}(\cdot)$ is the loss function commonly formulated in Frobenius-norm or Kullback-Leibler divergence.

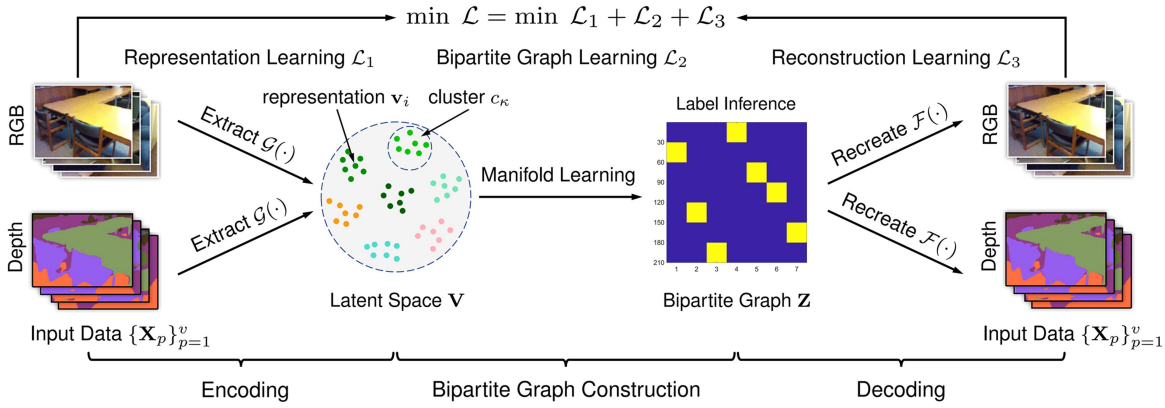

Fig. 3. Framework of BGAE. For simplicity, consider a two-view image dataset (RGB and Depth). The input data $\{\mathbf{X}_p\}_{p=1}^v$ are first encoded into a unified latent space by $\mathcal{G}(\cdot)$. Then, we construct a bipartite graph $\mathbf{Z}$ in the latent semantic space $\mathbf{V}$. Finally, the bipartite graph is decoded by $\mathcal{F}(\cdot)$ to recreate the input data. Therefore, our BGAE integrates "encoding", "bipartite graph construction", and "decoding" modules, i.e., jointly minimize representation learning loss $\mathcal{L}_1$, bipartite graph learning loss $\mathcal{L}_2$, and reconstruction learning loss $\mathcal{L}_3$, into a unified framework in graph machine learning settings.

TABLE I
BASIC NOTATIONS

Notation	Definition
n, v, k, m	Number of samples, views, clusters, anchors
d_p	Feature dimension for the p-th view
d	Latent feature dimension
$\boldsymbol{\alpha} \in \mathbb{R}^{v\times 1}$	View weights in "encoding" process
$\boldsymbol{\gamma} \in \mathbb{R}^{v\times 1}$	View weights in "decoding" process
$\mathbf{X}_p \in \mathbb{R}^{d_p\times n}$	Input data for the p-th view
$\mathbf{U}_p \in \mathbb{R}^{d_p\times d}$	Base matrix for input data $\mathbf{X}_p$
$\mathbf{V} \in \mathbb{R}^{d\times n}$	Consistent latent representation
$\mathbf{W}_p \in \mathbb{R}^{d_p\times m}$	Projection matrix
$\mathbf{A} \in \mathbb{R}^{d\times m}$	Anchor matrix
$\mathbf{Z} \in \mathbb{R}^{n\times m}$	Bipartite graph matrix
$\mathbf{S} \in \mathbb{R}^{(n+m)\times(n+m)}$	Augmented graph of $\mathbf{Z}$
$\widetilde{\mathbf{L}} \in \mathbb{R}^{(n+m)\times(n+m)}$	Normalized Laplacian matrix of $\mathbf{Z}$
$\mathbf{E}_p \in \mathbb{R}^{d_p\times n}$	Auxiliary variables in ADMM
$\boldsymbol{\Lambda}_p \in \mathbb{R}^{d_p\times n}$	ALM multipliers

Many variants [38], [39] have been derived based on the NMF backbone, widely used for extracting low-rank representation. Ding et al. [40] proposed semi-NMF by removing the constraint on base matrix $\mathbf{U}$, tackling the data with mixed-signs, i.e.,

$$\min_{\mathbf{U},\mathbf{V}} \|\mathbf{X}-\mathbf{U}\mathbf{V}\|_F^2 = \min_{\mathbf{U},\mathbf{V}} \sum_{i=1}^{n} \|\mathbf{x}_i - \mathbf{U}\mathbf{v}_i\|_2^2, \text{ s.t. } \mathbf{V}\geq 0. \tag{2}$$

Furthermore, Ding et al. [41] proposed a one-sided $\mathbf{V}$-orthogonal version to enlarge the diversity of the representation and hold the uniqueness of the solution, i.e.,

$$\min_{\mathbf{U},\mathbf{V}} \|\mathbf{X}-\mathbf{U}\mathbf{V}\|_F^2, \text{ s.t. } \mathbf{U}\geq 0, \mathbf{V}\geq 0, \mathbf{V}\mathbf{V}^\top = \mathbf{I}_d, \tag{3}$$

where d denotes the feature dimension of $\mathbf{V}$.

B. Bipartite Graph Construction

A bipartite graph describes the correlation between two separate sets of vertices, i.e., anchors/landmarks and instances. Given an instance set $\mathcal{X} = \{\mathbf{x}_1, \mathbf{x}_2, \ldots, \mathbf{x}_n\}$ and an anchor set $\mathcal{A} = \{\mathbf{a}_1, \mathbf{a}_2, \ldots, \mathbf{a}_m\}$, we can construct an undirected bipartite graph $\mathcal{Z} = (\mathcal{X}, \mathcal{A}, \mathcal{E}, \mathbf{Z})$ by building their edges $\mathcal{E}$, $\mathbf{Z}$ is the affinity matrix weighing the connections in $\mathcal{Z}$. Typically, anchors are selected in the original space with the intention of recovering the complete point cloud.

Based on this, various BGC methods are proposed [23], [25]. Particularly, the locality-preserving paradigm is popular with researchers, supposing that the original high-dimensional feature space actually lies in a low-dimensional manifold [42]. For the ith sample, jth anchor is connected as a neighbor with probability z_{ij}. Intuitively, the anchor-node pair with a shorter distance $\|\mathbf{x}_i - \mathbf{a}_j\|_2^2$ corresponds to a larger probability z_{ij}, which is expressed by

$$\min_{\mathbf{Z}} \sum_{i=1}^{n}\sum_{j=1}^{m} \|\mathbf{x}_i - \mathbf{a}_j\|_2^2 z_{ij} + \zeta z_{ij}^2,$$
$$\text{s.t. } \mathbf{Z}\mathbf{1}_m = \mathbf{1}_n,\ \mathbf{Z}\geq 0, \tag{4}$$

where ζ is a penalized parameter that can be tuned by grid search or pre-determined following the technique [43]. Typically, anchors $\mathbf{A}$ are selected by k-means [26] or heuristic sampling methods [21], [25].

Along this framework, Li et al. [25] proposed a structural bipartite graph fusion model coupled with Laplacian rank constraint. Nie et al. [44], and Chen et al. [24] introduced feature selection and re-weighting mechanisms to select valuable features. Lu et al. [45] designed a fusion scheme to refine the representation. Yan et al. [46] incorporated feature learning and pseudo-labels generated by the fused bipartite graph to seek project direction and refined the graph by manifold regularization.

III. METHODOLOGY

A. Motivation

Although various graph machine learning based MVBGC models are proposed to pursue a "nice" bipartite graph, they adopt a common design that constructs the bipartite graph directly from the input data via (4), which means that optimization merely involves an unidirectional "encoding" process. However,

"encoding-decoding" is a popular manner in unsupervised deep learning, and the most typical one is AE [28]. Enlightened by this, this section carefully transfers the insight from AE into graph machine learning, and presents a novel "auto-encoding" BGAE framework.

B. The Proposed BGAE Framework

First, we build an "encoding" module. In AE, the encoder plays a role in extracting discriminative embedding $\mathcal{G}(\cdot)$ by neutral networks [28], i.e., mapping the original high-dimensional data $\mathbf{X}$ into a low-dimensional semantic space $\mathcal{G}(\mathbf{X})$. Analogously, our encoding module is designed in a similar manner. Recall that NMF is widely applied for dimensionality reduction, which can be used to learn new representations [37]. However, an apparent deficiency of the standard NMF with F-norm is that it is sensitive to outliers. Concretely, the residual of each sample is measured in the squared form $\|\mathbf{x}^i - \mathbf{U}\mathbf{v}_i\|_2^2$. Therefore, several outliers with huge errors will easily prevail the objective [38]. Instead, we utilize $\ell_{2,1}$-norm [47] based on the orthogonal backbone. It is verified that $\ell_{2,1}$-norm is robust to noise or outliers, and can hold the row rotation invariance property [47]. Moreover, to maximally explore and fuse the discriminative information across multiple views, we learn the latent joint representation. Therefore, our encoding module (representation learning loss $\mathcal{L}_1$) is formulated as

$$\begin{aligned}\min\ \mathcal{L}_1 :\ &\min_{\boldsymbol{\alpha},\mathbf{U}_p,\mathbf{V}}\ \sum_{p=1}^{v}\alpha_p^2\|\mathbf{X}_p-\mathbf{U}_p\mathbf{V}\|_{2,1},\\ &=\min_{\boldsymbol{\alpha},\mathbf{U}_p,\mathbf{V}}\ \sum_{p=1}^{v}\sum_{i=1}^{n}\alpha_p^2\left\|\mathbf{x}_p^i-\mathbf{U}_p\mathbf{v}_i\right\|_2,\\ &\text{s.t.}\ \begin{cases}\boldsymbol{\alpha}^\top\mathbf{1}=1,\ \alpha_p\geq 0,\\ \mathbf{V}\mathbf{V}^\top=\mathbf{I}_d.\end{cases}\end{aligned}\tag{5}$$

where $\mathbf{V}$ is the latent consistent representation, $\mathbf{U}_p$ is the view-specific base matrix, and α_p measures the contribution of different views. Actually, (5) is to impose ℓ_2-norm within a sample and ℓ_1-norm among all instances across multiple views. Compared to F-norm, $\ell_{2,1}$-norm measures residuals by non-squared $\|\mathbf{x}_p^i-\mathbf{U}_p\mathbf{v}_i\|_2$, reducing the impact of outliers. Note that we relax the non-negative constraints, which enlarge the feasible region to fully explore the intrinsic structures of input data with mixed-signs.

Then, we build a bipartite graph construction module. Considering that the latent representation integrates the discriminative information of the input data, we construct a bipartite graph with locality-preserving property in the latent semantic space instead of the original space as existing methods do. Such a module (bipartite graph construction loss $\mathcal{L}_2$) is formulated as

$$\begin{aligned}\min\ \mathcal{L}_2 :\ &\min_{\mathbf{A},\mathbf{Z}}\ \sum_{i=1}^{n}\sum_{j=1}^{m}\|\mathbf{v}_i-\mathbf{a}_j\|_2^2\,z_{ij},\\ &\text{s.t.}\ \mathbf{Z}\mathbf{1}_m=\mathbf{1}_n,\ \mathbf{Z}\geq 0,\end{aligned}\tag{6}$$

where $\mathbf{Z}$ is the bipartite graph and $\mathbf{A}$ is the anchors learned by constraint-free optimization.

Finally, we elaborate on how to build the "decoding" module. In AE, the decoder recreates the input data from the encoded representation via neural networks, i.e., $\mathcal{F}(\mathcal{G}(\mathbf{X}))$. However, in traditional settings, *the first core question is which variable should be used to recreate the input data, the latent representation* $\mathbf{V}$ *or the bipartite graph* $\mathbf{Z}$*?* The former choice is likely to be a "close to perfect" duplication of $\mathbf{X}$, since $\mathbf{V}$ is just extracted from $\mathbf{X}$ in (5), duplication is meaningless for bipartite graph optimization. In deep learning, standard AE also notices this problem and derives undercomplete AE for message compression and dimensionality reduction [28]. Enlightened by this, we should design an undercomplete "auto-encoding" framework instead of perfectly recreating the input data, so that the latter choice is more reasonable and practical. Furthermore, *the second core question is how to recreate the input data by the bipartite graph?* The inconsistent sizes of $\mathbf{Z}$ and $\{\mathbf{X}_p\}_{p=1}^v$ make it difficult to build their correlation. For simplicity, we introduce orthogonal projection to hold their consistent feature dimension, thus the "decoding" module (reconstruction loss $\mathcal{L}_3$) is formulated as

$$\begin{aligned}\min\ \mathcal{L}_3 :\ &\min_{\boldsymbol{\gamma},\mathbf{Z},\mathbf{W}_p}\ \sum_{p=1}^{v}\gamma_p^2\left\|\mathbf{W}_p\mathbf{Z}^\top-\mathbf{X}_p\right\|_F^2,\\ &\text{s.t.}\ \begin{cases}\boldsymbol{\gamma}^\top\mathbf{1}=1,\ \gamma_p\geq 0,\\ \mathbf{Z}\mathbf{1}_m=\mathbf{1}_n,\ \mathbf{Z}\geq 0,\\ \mathbf{W}_p^\top\mathbf{W}_p=\mathbf{I}_m,\end{cases}\end{aligned}\tag{7}$$

where $\mathbf{W}_p$ is the projection matrices, γ_p measures the capacity of bipartite graph $\mathbf{Z}$ to recreate input data.

So far, we have carefully presented our motivation and technical route. Note that loss of AE is to measure the discrepancy between the input data and the reconstructed representation via neural networks, i.e., $\mathcal{L}(\mathbf{X},\mathcal{F}(\mathcal{G}(\mathbf{X})))$. However, in traditional machine learning scenarios, it is difficult to exactly follow such a setting. For simplicity, we directly combine the three losses $\mathcal{L}=\mathcal{L}_1+\mathcal{L}_2+\mathcal{L}_3$. In addition, we introduce Laplacian rank constraint to enforce the bipartite graph holds clear k-connected components, so that it can naturally infer discrete labels without any post-processing. Our novel end-to-end "auto-encoding" BGAE framework is as follows,

$$\begin{aligned}&\min\ \mathcal{L}_1+\mathcal{L}_2+\mathcal{L}_3:\\ &\min_{\substack{\boldsymbol{\alpha},\boldsymbol{\gamma},\mathbf{U}_p,\mathbf{V},\\ \mathbf{A},\mathbf{Z},\mathbf{W}_p}}\ \underbrace{\sum_{p=1}^{v}\alpha_p^2\|\mathbf{X}_p-\mathbf{U}_p\mathbf{V}\|_{2,1}}_{Encoding}\\ &\quad+\underbrace{\sum_{i=1}^{n}\sum_{j=1}^{m}\|\mathbf{v}_i-\mathbf{a}_j\|_2^2\,z_{ij}}_{Bipartite\ Graph\ Construction}\\ &\quad+\underbrace{\sum_{p=1}^{v}\gamma_p^2\left\|\mathbf{W}_p\mathbf{Z}^\top-\mathbf{X}_p\right\|_F^2}_{Decoding},\end{aligned}$$

$$\text{s.t.} \begin{cases} \boldsymbol{\alpha}^\top \mathbf{1} = 1,\ \alpha_p \geq 0, \\ \boldsymbol{\gamma}^\top \mathbf{1} = 1,\ \gamma_p \geq 0, \\ \mathbf{V}\mathbf{V}^\top = \mathbf{I}_d, \\ \mathbf{Z}\mathbf{1}_m = \mathbf{1}_n,\ \mathbf{Z} \geq 0, \\ \mathbf{W}_p^\top \mathbf{W}_p = \mathbf{I}_m, \\ rank(\widetilde{\mathbf{L}}) = n + m - k, \end{cases} \tag{8}$$

where $\widetilde{\mathbf{L}} = \mathbf{I} - \mathbf{D}^{-\frac{1}{2}}\mathbf{S}\mathbf{D}^{-\frac{1}{2}}$ denotes the normalized Laplacian matrix of $\mathbf{S} \in \mathbb{R}^{(n+m)\times(n+m)}$, $\mathbf{S}$ and $\mathbf{D}$ are the augmented graph and diagonal matrix of $\mathbf{Z}$ defined by

$$\mathbf{S} = \begin{bmatrix} \mathbf{0} & \mathbf{Z} \\ \mathbf{Z}^\top & \mathbf{0} \end{bmatrix},\ \mathbf{D} = \begin{bmatrix} \mathbf{D}_n & \mathbf{0} \\ \mathbf{0} & \mathbf{D}_m \end{bmatrix}, \tag{9}$$

where $\mathbf{D}_n = diag(\mathbf{Z}\mathbf{1}) = \mathbf{I}_n$ and $\mathbf{D}_m = diag(\mathbf{Z}^\top \mathbf{1}) \in \mathbb{R}^{m\times m}$. As noted in [25], Lemma 1 and Remark 1 illustrate that such a connectivity constraint can guarantee clear k-connected components of $\mathbf{S}$ and $\mathbf{Z}$, and each component naturally corresponds to a disjoint cluster.

Lemma 1: The multiplicity of eigenvalue zeros of the normalized Laplacian matrix $\widetilde{\mathbf{L}}$ equals the number of connected components in the graph associated with $\mathbf{S}$.

Remark 1: The augmented graph $\mathbf{S}$ consists of a bipartite graph matrix $\mathbf{Z}$ and its transposed form $\mathbf{Z}^\top$. $\mathbf{S}$ and $\mathbf{Z}$ share the same number of connected components.

Remark 2: Note that (6) does not adhere to the standard bipartite graph learning paradigm in (4) as we remove the regularizer $\zeta \sum_{i=1}^{n}\sum_{j=1}^{m} z_{ij}^2 = \zeta \mathrm{Tr}(\mathbf{Z}\mathbf{Z}^\top)$, where ζ is a hyper-parameter requiring fine-tuning or heuristic method [43]. The reason is that (7) inherently incorporates $\gamma_p^2 \mathrm{Tr}(\mathbf{Z}\mathbf{Z}^\top)$, which naturally plays a role of avoiding the sparse trivial solution. Furthermore, γ_p can be optimized instead of the time-consuming parameter-tuning process induced by η.

In summary, this section proposes a novel MVBGC design, termed "auto-encoding" BGAE. The encoding module extracts a latent representation across multiple views. The bipartite graph construction module introduces manifold graph learning to explore intrinsic geometrical structures. The decoding module recreates the input data via bipartite graph, which provides feedback to learning process that allows bipartite graph not far from the input multi-view data, enforcing it contains complementary information. Therefore, by jointly minimizing $\mathcal{L} = \mathcal{L}_1 + \mathcal{L}_2 + \mathcal{L}_3$, the bipartite graph balances consistency and complementary properties across all views, which is a vital pursuit in multi-view learning [34], [48]. Compared to most existing models that only consider encoding input data into bipartite graphs by (4), our novel design achieves end-to-end "encoding-decoding" bipartite graph machine learning.

C. Optimization Algorithm

Since we impose $\ell_{2,1}$-norm, orthogonal constraint, and Laplacian rank constraint, it is difficult to solve the model directly. This section designs an ADMM solver.

First, we derive the matrix form of (6), i.e.,

$$\begin{aligned} &\sum_{i=1}^{n}\sum_{j=1}^{m} \|\mathbf{v}_i - \mathbf{a}_j\|_2^2 z_{ij} \\ &= \sum_{i=1}^{n}\sum_{j=1}^{m} (\mathbf{v}_i - \mathbf{a}_j)^\top (\mathbf{v}_i - \mathbf{a}_j) z_{ij} \\ &= \sum_{i=1}^{n} \mathbf{v}_i^\top \left(\sum_{j=1}^{m} z_{ij}\right) \mathbf{v}_i - 2\sum_{i=1}^{n}\sum_{j=1}^{m} \mathbf{v}_i^\top z_{ij} \mathbf{a}_j \\ &\quad + \sum_{j=1}^{m} \mathbf{a}_j{}^\top \left(\sum_{i=1}^{n} z_{ij}\right) \mathbf{a}_j \\ &= \mathrm{Tr}\left(\mathbf{V}\mathbf{D}_n\mathbf{V}^\top - 2\mathbf{V}\mathbf{Z}\mathbf{A}^\top + \mathbf{A}\mathbf{D}_m\mathbf{A}^\top\right) \end{aligned} \tag{10}$$

Then, considering that the non-convex Laplacian rank constraint is difficult to deal with, we solve it with a relaxed solution. Denoting $\sigma_i(\widetilde{\mathbf{L}})$ is the ith smallest eigenvalue of $\widetilde{\mathbf{L}}$. Note that $\widetilde{\mathbf{L}}$ satisfies semi-definite property, i.e., $\sigma_i(\widetilde{\mathbf{L}}) \geq 0$. Once rank-$k$ smallest $\sigma_i(\widetilde{\mathbf{L}})$ equals zero, the rank constraint will be achieved, and $\mathbf{S}$ will be an ideal graph preserving clear k-connected components structures. According to Ky Fan's Theorem [49], we have $\sum_{i=1}^{k}\sigma_i(\widetilde{\mathbf{L}}) = \min_{\mathbf{F}^\top\mathbf{F}=\mathbf{I}_k} \mathrm{Tr}(\mathbf{F}^\top\widetilde{\mathbf{L}}\mathbf{F})$, where $\mathbf{F} \in \mathbb{R}^{(n+m)\times k}$ denotes the graph embedding.

Finally, by introducing v auxiliary variables $\{\mathbf{E}_p = \mathbf{X}_p - \mathbf{U}_p\mathbf{V}\}_{p=1}^{v}$ to separate constraints and hold equivalence during optimization, our model is transformed into the following Augmented Lagrangian Multiplier (ALM) problem

$$\begin{aligned} \min_{\substack{\boldsymbol{\alpha},\boldsymbol{\gamma},\mathbf{U}_p,\mathbf{V},\mathbf{A},\\ \mathbf{Z},\mathbf{F},\mathbf{W}_p,\mathbf{E}_p,\boldsymbol{\Lambda}_p}} & \sum_{p=1}^{v} \alpha_p^2 \|\mathbf{E}_p\|_{2,1} \\ & + \mathrm{Tr}\left(\mathbf{V}\mathbf{D}_n\mathbf{V}^\top - 2\mathbf{V}\mathbf{Z}\mathbf{A}^\top + \mathbf{A}\mathbf{D}_m\mathbf{A}^\top\right) \\ & + \sum_{p=1}^{v} \gamma_p^2 \left\|\mathbf{W}_p\mathbf{Z}^\top - \mathbf{X}_p\right\|_F^2 + \mu\mathrm{Tr}\left(\mathbf{F}^\top\widetilde{\mathbf{L}}\mathbf{F}\right) \\ & + \frac{\beta}{2}\sum_{p=1}^{v}\left\|\mathbf{X}_p - \mathbf{U}_p\mathbf{V} - \mathbf{E}_p + \frac{1}{\beta}\boldsymbol{\Lambda}_p\right\|_F^2, \\ \text{s.t.} & \begin{cases} \boldsymbol{\alpha}^\top \mathbf{1} = 1,\ \alpha_p \geq 0, \\ \boldsymbol{\gamma}^\top \mathbf{1} = 1,\ \gamma_p \geq 0, \\ \mathbf{V}\mathbf{V}^\top = \mathbf{I}_d, \\ \mathbf{Z}\mathbf{1}_m = \mathbf{1}_n,\ \mathbf{Z} \geq 0, \\ \mathbf{W}_p^\top\mathbf{W}_p = \mathbf{I}_m, \\ \mathbf{F}^\top\mathbf{F} = \mathbf{I}_k, \end{cases} \end{aligned} \tag{11}$$

where $\{\boldsymbol{\Lambda}_p\}_{p=1}^{v}$ are ALM multipliers to penalize the discrepancy between the original objective and the introduced auxiliary variable, μ is a penalized parameter that should be large enough to hold the rank-k smallest $\sigma_i(\widetilde{\mathbf{L}})$ infinitely close to zero, and β is the ALM parameter.

We optimize (11) by block-coordinate descent strategy that alternately updates each variable with others being fixed. Algorithm 1 summarizes the overall workflow.

1) Update $\mathbf{U}_p$: With others being fixed, each $\mathbf{U}_p$ is solved by

$$\min_{\mathbf{U}_p} \frac{\beta}{2}\sum_{p=1}^{v}\left\|\mathbf{X}_p - \mathbf{U}_p\mathbf{V} - \mathbf{E}_p + \frac{1}{\beta}\boldsymbol{\Lambda}_p\right\|_F^2. \tag{12}$$

Since no constraint is imposed on $\mathbf{U}_p$ and $\mathbf{V}\mathbf{V}^\top = \mathbf{I}_d$, each $\mathbf{U}_p$ can be updated independently by

$$\min_{\mathbf{U}_p} \left\| \mathbf{U}_p - \left(\mathbf{X}_p - \mathbf{E}_p + \frac{1}{\beta}\mathbf{\Lambda}_p \right) \mathbf{V}^\top \right\|_F^2. \tag{13}$$

Clearly, we have

$$\mathbf{U}_p = \left(\mathbf{X}_p - \mathbf{E}_p + \frac{1}{\beta}\mathbf{\Lambda}_p \right) \mathbf{V}^\top. \tag{14}$$

2) Update $\mathbf{V}$*:* With others being fixed, $\mathbf{V}$ can be solved by

$$\max_{\mathbf{V}} \ \mathrm{Tr}\left(\mathbf{V}\mathbf{M}\right), \ \text{s.t.}\ \mathbf{V}\mathbf{V}^\top = \mathbf{I}_d, \tag{15}$$

where $\mathbf{M} = 2\mathbf{Z}\mathbf{A}^\top + \beta \sum_{p=1}^{v} \mathbf{Q}_p^\top \mathbf{U}_p$ and $\mathbf{Q}_p = \mathbf{X}_p - \mathbf{E}_p + \frac{1}{\beta}\mathbf{\Lambda}_p$. The analytical solution can be achieved by singular value decomposition (SVD) [22].

3) Update $\mathbf{Z}$*:* With others being fixed, $\mathbf{Z}$ is solved by

$$\begin{aligned} \min_{\mathbf{Z},\mathbf{F}} \ \mathrm{Tr} \Bigg(& \sum_{p=1}^{v} \gamma_p^2 \mathbf{Z}^\top \mathbf{Z} + \mathbf{1}_n \left(diag\left(\mathbf{A}^\top \mathbf{A}\right)^\top \right) \mathbf{Z}^\top \\ & -2\mathbf{V}^\top \mathbf{A}\mathbf{Z}^\top - 2\sum_{p=1}^{v} \gamma_p^2 \mathbf{X}_p^\top \mathbf{W}_p \mathbf{Z}^\top \Bigg) + \mu \mathrm{Tr}\left(\mathbf{F}^\top \widetilde{\mathbf{L}} \mathbf{F} \right), \\ \text{s.t.}\ & \mathbf{Z}\mathbf{1}_m = \mathbf{1}_n, \ \mathbf{Z} \geq 0, \ \mathbf{F}^\top \mathbf{F} = \mathbf{I}_k. \end{aligned} \tag{16}$$

Since (16) involves two variables, we use the block-coordinate descent method to update $\mathbf{Z}$ and $\mathbf{F}$ alternatively. With $\mathbf{Z}$ being fixed, (16) is simplified to,

$$\min_{\mathbf{F}} \ \mathrm{Tr}\left(\mathbf{F}^\top \widetilde{\mathbf{L}} \mathbf{F} \right), \text{s.t.}\ \mathbf{F}^\top \mathbf{F} = \mathbf{I}_k. \tag{17}$$

To efficiently solve (17), we solve the singular values of $\mathbf{Z}$ rather than the eigenvalues of $\mathbf{S}$. By decomposing $\mathbf{F} = \begin{bmatrix} \mathbf{F}_n \\ \mathbf{F}_m \end{bmatrix}$, (17) can be rewritten as,

$$\begin{aligned} \max_{\mathbf{F}_n,\mathbf{F}_m} \ & \mathrm{Tr}\left(\mathbf{F}_n^\top \mathbf{D}_n^{-\frac{1}{2}} \mathbf{Z} \mathbf{D}_m^{-\frac{1}{2}} \mathbf{F}_m \right), \\ & \text{s.t.}\ \mathbf{F}_n^\top \mathbf{F}_n + \mathbf{F}_m^\top \mathbf{F}_m = \mathbf{I}_k. \end{aligned} \tag{18}$$

Theorem 1 provides the analytical solution of (18).

Theorem 1: Supposing $\mathbf{P} \in \mathbb{R}^{n\times k}, \mathbf{O} \in \mathbb{R}^{n\times m}, \mathbf{R} \in \mathbb{R}^{m\times k}$, we have

$$\begin{aligned} \max_{\mathbf{P},\mathbf{R}} \ & \mathrm{Tr}\left(\mathbf{P}^\top \mathbf{O} \mathbf{R} \right), \\ & \text{s.t.}\ \mathbf{P}^\top \mathbf{P} + \mathbf{R}^\top \mathbf{R} = \mathbf{I}_k. \end{aligned} \tag{19}$$

The optimal solutions are $\mathbf{P} = \frac{\sqrt{2}}{2}\mathbf{U_o}$ and $\mathbf{R} = \frac{\sqrt{2}}{2}\mathbf{V_o}$, where $\mathbf{U_o}$ and $\mathbf{V_o}$ are the rank-k left and right singular vectors of $\mathbf{O}$.

Detailed proof is provided in supplementary material, available online.

After optimizing $\mathbf{F}$, we turn to optimize $\mathbf{Z}$. We have

$$\mathrm{Tr}\left(\mathbf{F}^\top \widetilde{\mathbf{L}} \mathbf{F} \right) = \sum_{i=1}^{n} \sum_{j=1}^{m} t_{ij} z_{ij} = \mathrm{Tr}\left(\mathbf{T}\mathbf{Z}^\top \right), \tag{20}$$

where $t_{ij} = \| \frac{\mathbf{f}_n^i}{\sqrt{\mathbf{D}_{n[i,i]}}} - \frac{\mathbf{f}_m^j}{\sqrt{\mathbf{D}_{m[j,j]}}} \|_2^2$.

Eq. (16) can be rewritten as n row independent problem w.r.t. $\mathbf{Z}$, i.e.,

$$\begin{aligned} \min_{\mathbf{Z}_{[i,:]}} \ & \frac{1}{2} \left\| \mathbf{Z}_{[i,:]} - \widetilde{\mathbf{Z}}_{[i,:]} \right\|_2^2, \\ & \text{s.t.}\ \mathbf{Z}_{[i,:]}\mathbf{1} = 1, \ \mathbf{Z}_{[i,:]} \geq 0, \end{aligned} \tag{21}$$

where $\widetilde{\mathbf{Z}}_{[i,:]} = -\frac{\mathbf{g}^\top}{2\sum_{p=1}^{v}\gamma_p^2}$, $\mathbf{g}^\top = diag(\mathbf{A}^\top\mathbf{A})^\top - (2\mathbf{V}^\top\mathbf{A} + 2\sum_{p=1}^{v}\gamma_p^2\mathbf{X}_p^\top\mathbf{W}_p - \mu\mathbf{T})_{[i,:]}$.

Theorem 2 gives the analytical solution of (21).

Theorem 2: The analytical solution of (21) is

$$\mathbf{Z}_{[i,:]} = \left(\widetilde{\mathbf{Z}}_{[i,:]} + \epsilon_i \mathbf{1}_m^\top \right)_+, \tag{22}$$

where ϵ_i can be solved by Newton's method efficiently.

Detailed proof is provided in [22].

4) Update $\mathbf{E}_p$*:* With others being fixed, each $\mathbf{E}_p$ is independently solved by

$$\min_{\mathbf{E}_p} \ \alpha_p^2 \left\| \mathbf{E}_p \right\|_{2,1} + \frac{\beta}{2} \| \mathbf{X}_p - \mathbf{U}_p\mathbf{V} - \mathbf{E}_p + \frac{1}{\beta}\mathbf{\Lambda}_p \|_F^2, \tag{23}$$

which can be further rewritten as the following compact formulation

$$\min_{\mathbf{E}_p} \ \frac{\alpha_p^2}{\beta} \left\| \mathbf{E}_p \right\|_{2,1} + \frac{1}{2} \| \mathbf{E}_p - \mathbf{H}_p \|_F^2, \tag{24}$$

where $\mathbf{H}_p = \mathbf{X}_p - \mathbf{U}_p\mathbf{V} + \frac{1}{\beta}\mathbf{\Lambda}_p$. According to [39], the solution is

$$\mathbf{e}_p^i = \begin{cases} \left(1 - \frac{\alpha_p^2}{\beta \| \mathbf{h}_p^i \|_2} \right) \mathbf{h}_p^i, & if \ \left\| \mathbf{h}_p^i \right\|_2 > \frac{\alpha_p^2}{\beta}, \\ 0, & otherwise. \end{cases} \tag{25}$$

5) Update $\mathbf{A}$*:* With others being fixed, $\mathbf{A}$ is solved by

$$\min_{\mathbf{A}} \mathrm{Tr}\left(-2\mathbf{V}\mathbf{Z}\mathbf{A}^\top + \mathbf{A}\mathbf{D}_m\mathbf{A}^\top \right). \tag{26}$$

Taking the partial derivative on $\mathbf{A}$, we have

$$\begin{aligned} & \frac{\partial}{\partial \mathbf{A}} \mathrm{Tr}\left(-2\mathbf{V}\mathbf{Z}\mathbf{A}^\top + \mathbf{A}\mathbf{D}_m\mathbf{A}^\top \right) \\ & \quad = -2\mathbf{V}\mathbf{Z} + 2\mathbf{A}\mathbf{D}_m. \end{aligned} \tag{27}$$

By enforcing the partial derivative equals to 0, we have

$$\mathbf{V}\mathbf{Z} = \mathbf{A}\mathbf{D}_m. \tag{28}$$

Supposing $(\mathbf{D}_m)^{-1}$ exists, we have

$$\mathbf{A} = \mathbf{V}\mathbf{Z}(\mathbf{D}_m)^{-1}. \tag{29}$$

Remark 3: $(\mathbf{D}_m)^{-1}$ exists means that the column sum of the bipartite graph $\mathbf{Z} \in \mathbb{R}^{n\times m}$ are always greater than 0. However, such ideal cases do not always hold, and there is still a minimal probability that the jth column sum of $\mathbf{Z}$ is 0 in experiments. That is, $\mathbf{a}_j$ is an isolated anchor without building membership with other instances. In experiments, we find that such undesirable cases may occur during inchoate iterations, and the existence of isolated $\mathbf{a}_j$ has no impact on the objective value, so it will not affect exploring the final graph representation. Therefore, we remove the isolated anchors directly.

Algorithm 1: BGAE.

Input: Input data $\{\mathbf{X}_p\}_{p=1}^v$, cluster number k, anchor number m, latent dimension d, maximal iteration Γ.
Initialize $\{\mathbf{U}_p\}_{p=1}^v$, $\mathbf{A}$, $\{\mathbf{W}_p\}_{p=1}^v$, $\mathbf{Z}$, $\mathbf{V}$, $\boldsymbol{\alpha}$, $\boldsymbol{\gamma}$, $\{\boldsymbol{\Lambda}_p\}_{p=1}^v$.
while not converged and iteration less than Γ **do**
  Optimize $\{\mathbf{E}_p\}_{p=1}^v$ by updating (23).
  Optimize $\{\mathbf{U}_p\}_{p=1}^v$ by updating (12).
  Optimize $\mathbf{A}$ by updating (26).
  Optimize $\{\mathbf{W}_p\}_{p=1}^v$ by updating (30).
  Optimize $\mathbf{Z}$ by updating (16).
  Optimize $\mathbf{V}$ by updating (15).
  Optimize $\boldsymbol{\alpha}$ by updating (31).
  Optimize $\boldsymbol{\gamma}$ by updating (33).
  Optimize $\{\boldsymbol{\Lambda}_p\}_{p=1}^v$ and β by updating (35).
end while
Output: The predicted clustering labels $\widetilde{\mathbf{Y}}$.

6) Update $\mathbf{W}_p$: With others being fixed, each $\mathbf{W}_p$ is solved by

$$\max_{\mathbf{W}_p} \operatorname{Tr}\left(\mathbf{W}_p^\top \mathbf{B}_p\right), \text{ s.t. } \mathbf{W}_p^\top \mathbf{W}_p = \mathbf{I}_m, \tag{30}$$

where $\mathbf{B}_p = \mathbf{X}_p\mathbf{Z}$, (30) can be efficiently solved by SVD.

7) Update $\boldsymbol{\alpha}$: With other variables being fixed, each α_p is independently optimized by

$$\min_{\alpha_p} \sum_{p=1}^{v} \alpha_p^2 \tau_p, \text{ s.t. } \boldsymbol{\alpha} \geq 0, \boldsymbol{\alpha}^\top \mathbf{1} = 1, \tag{31}$$

where $\tau_p = \|\mathbf{X}_p - \mathbf{U}_p\mathbf{V}\|_{2,1}$. The solution of α_p can be straightly computed by Cauchy-Schwarz inequality, i.e.,

$$\alpha_p = \frac{1/\tau_p}{\sum_{p=1}^{v} 1/\tau_p}. \tag{32}$$

8) Update $\boldsymbol{\gamma}$: With other variables being fixed, each γ_p is independently optimized by

$$\min_{\gamma_p} \sum_{p=1}^{v} \gamma_p^2 \delta_p, \text{ s.t. } \boldsymbol{\gamma} \geq 0, \boldsymbol{\gamma}^\top \mathbf{1} = 1, \tag{33}$$

where $\delta_p = \|\mathbf{W}_p\mathbf{Z}^\top - \mathbf{X}_p\|_F^2$. The solution of γ_p can be straightly computed by Cauchy-Schwarz inequality, i.e.,

$$\gamma_p = \frac{1/\delta_p}{\sum_{p=1}^{v} 1/\delta_p}. \tag{34}$$

9) Update $\boldsymbol{\Lambda}_p$ and β: Each Lagrangian multiplier $\boldsymbol{\Lambda}_p$ and β can be updated by

$$\begin{aligned} \boldsymbol{\Lambda}_p &= \boldsymbol{\Lambda}_p + \beta\left(\mathbf{X}_p - \mathbf{U}_p\mathbf{V} - \mathbf{E}_p\right), \\ \beta &= \rho\beta, \end{aligned} \tag{35}$$

where ρ controls the convergence speed and we empirically set $\rho = 2$ in experiments.

TABLE II
MVC DATASETS STATISTICS

Dataset	Samples	Views	Clusters	Feature Dims
Yale	165	3	15	4,096/3,304/6,750
3sources	169	3	6	3,560/3,631/3,068
MSRCV1	210	6	7	1,302/48/512/100/256/210
Dermatology	358	2	6	12/22
ORL_3views	400	3	40	4,096/3,304/6,750
ORL_4views	400	4	40	256/256/256/256
SUN RGB-D	10,335	2	45	4,096/4,096
YouTubeFace20	63,896	4	20	944/576/512/640
YouTubeFace50	126,054	4	50	944/576/512/640
YouTubeFace100	195,537	4	100	944/576/512/640

D. Complexity Analysis

In graph machine learning, constructing similarity graphs is necessary. Given a desktop with 64 GB RAM, a double precision floating point format requires 8 bytes, the largest matrix that can be stored is $92,682 \times 92,682$, and larger sizes will incur out-of-memory error. This section carefully analyses the complexities. For simplicity, we set $g_1 = \sum_{p=1}^{v} d_p$ and $g_2 = \sum_{p=1}^{v} d_p^2$. Commonly, $n \gg d$ and $n \gg m$.

Time Complexity: The time complexity consists of nine parts: (1) updating $\{\mathbf{E}_p\}_{p=1}^v$ requires $\mathcal{O}(ng_1d)$ complexity, (2) updating $\{\mathbf{U}_p\}_{p=1}^v$ requires $\mathcal{O}(ng_1d)$ complexity, (3) updating $\mathbf{A}$ requires $\mathcal{O}(ndm)$ complexity, (4) updating $\{\mathbf{W}_p\}_{p=1}^v$ requires $\mathcal{O}(n(g_1m + g_2))$ complexity, (5) updating $\mathbf{Z}$ requires $\mathcal{O}(n(g_1m + dm + m^2))$ complexity, (6) updating $\mathbf{V}$ requires $\mathcal{O}(n(g_1m + dm + d^2))$ complexity, (7) updating $\boldsymbol{\alpha}$ requires $\mathcal{O}(ng_1d)$ complexity, (8) updating $\boldsymbol{\gamma}$ requires $\mathcal{O}(n(g_1m + g_2))$ complexity, (9) updating $\{\boldsymbol{\Lambda}_p\}_{p=1}^v$ requires $\mathcal{O}(ng_1d)$ complexity. So, the total time complexity for each iteration is $\mathcal{O}(n(g_1d + g_1m + g_2 + dm + d^2 + m^2))$.

Space Complexity: The space complexity comes from storing huge matrices, i.e., $\{\mathbf{E}_p\}_{p=1}^v$, $\{\mathbf{X}_p\}_{p=1}^v$, $\{\mathbf{U}_p\}_{p=1}^v$, $\mathbf{A}$, $\{\mathbf{W}_p\}_{p=1}^v$, $\mathbf{Z}$, $\mathbf{V}$, and $\{\boldsymbol{\Lambda}_p\}_{p=1}^v$. The total space complexity is $\mathcal{O}(n(g_1 + d + m) + g_1(d + m) + dm)$.

Therefore, the complexities are linear with n, enabling it can scale to large datasets with $n \geq 100,000$.

IV. EXPERIMENT

A. Experimental Settings

1) Synthetic Datasets: To visualize the "benefits" from the "decoding" learning in retaining the initial manifold structures, we design a synthetic two-moon data from two clusters, shown in Fig. 2(a). Each moon consists of 100 samples, one moon is colored with green dots and the other with pink dots.

2) Realistic Datasets: Table II lists ten public MVC datasets. Yale[1] involves 165 grayscale images of 15 individuals. 3sources[2] is a text dataset. MSRCV1 [58] contains 210 images from 7 clusters. ORL_3views and ORL_4views[3] are face datasets containing 400 images from 40 categories but with different

[1] http://cvc.cs.yale.edu/cvc/projects/yalefaces/yalefaces.html
[2] http://mlg.ucd.ie/datasets/3sources.html
[3] https://cam-orl.co. UK/facedatabase.html

TABLE III
COMPARISON OF ALGORITHM COMPLEXITY

Method	Space Complexity	Time Complexity
RMKM [50]	$\mathcal{O}(n^2+n(g_1+k)+g_1k)$	$\mathcal{O}(n^2)$
AMGL [51]	$\mathcal{O}(n^2v+n(g_1+k))$	$\mathcal{O}(n^3)$
FMR [52]	$\mathcal{O}(n^2+n(g_1+k))$	$\mathcal{O}(n^3)$
PMSC [53]	$\mathcal{O}(n^2v+n(g_1+kv))$	$\mathcal{O}(n^3)$
BMVC [54]	$\mathcal{O}((n+d_{mean})l)$	$\mathcal{O}(n)$
LMVSC [26]	$\mathcal{O}(n(g_1+mv)+g_1mv)$	$\mathcal{O}(n)$
SMVSC [18]	$\mathcal{O}(nm+(g_1+m)k)$	$\mathcal{O}(n)$
SFMC [25]	$\mathcal{O}(n(g_1+mv))$	$\mathcal{O}(n)$
FMCNOF [55]	$\mathcal{O}(n(g_1+mv+k)+mk)$	$\mathcal{O}(n)$
FPMVS [56]	$\mathcal{O}(nk+(g_1+k)k)$	$\mathcal{O}(n)$
SDAFG [45]	$\mathcal{O}(n(g_1+mv))$	$\mathcal{O}(n)$
UDBGL [57]	$\mathcal{O}(n(g_1+mv)+g_1m)$	$\mathcal{O}(n)$
FastMICE [21]	$\mathcal{O}(n(g_1+k+k_{neibor}+m+v))$	$\mathcal{O}(n)$
Proposed	$\mathcal{O}(n(g_1+d+m)+g_1(d+m)+dm)$	$\mathcal{O}(n)$

views. SUN RGB-D[4] contains 10,335 real RGB-D images of room scenes. YouTubeFace20, YouTubeFace50, and YouTubeFace100 are face video datasets extracted from YouTube [21] with different number of clusters.

3) Compared Baselines: To evaluate the effectiveness of the proposed BGAE framework, thirteen state-of-the-art baselines are collected. 1) RMKM [50] proposes a robust MVC method using $\ell_{2,1}$-norm. 2) AMGL [51] designs a multi-graph clustering model with an auto-weighted strategy. 3) FMR [52] introduces kernel dependence measure to extract latent representation with nonlinear and high-order structures. 4) PMSC [53] fuses multiple views in the partition level. 5) BMVC [54] incorporates collaborative binary coding and binary cluster structure learning. 6) LMVSC [26] proposes sampling anchors by k-means and concatenating multiple anchor graphs to exploit complementary information. 7) SMVSC [18] proposes to project multiple views into a latent space and learn unified anchors through optimization. 8) SFMC [25] restricts generating the same anchors across multiple views and fuses a unified bipartite graph with Laplacian rank constraint. 9) FMCNOF [55] designs an orthogonal NMF variant and fuses a unified indicator matrix to predict labels directly. 10) FPMVS [56] is a parameter-free extension of SMVSC. 11) SDAFG [45] exploits structural diversity by merging diverse anchor graphs into a large target graph with connectivity constraints. 12) UDBGL [57] fuses view-wise and view-consensus information to learn a unified anchor graph and coupled with connectivity constraints to hold discrete cluster structures. 13) FastMICE [21] introduces the concept of random view groups to capture multi-view relationships and devises a hybrid fusion method to combine diversities of features, anchors, and neighbors, achieving ensemble clustering. Table III reports their complexity.

4) Technical Details: The codes of compared baselines are collected directly from the authors' homepage or GitHub without corrections, hyper-parameters are carefully tuned following the authors' suggestions, and we report the best metrics. For baselines involving k-means, the results mean $\pm$ std are reported by repeating 50 times to alleviate randomness. The cluster number k is assumed pre-known following most experimental settings [59], [60], [61].

[4]https://rgbd.cs.princeton.edu/

For our BGAE, the anchor number m is fixed at k, the latent dimension d of representation $\mathbf{V}$ varies in $[k, 2k, \ldots, 9k]$ and $d \leq \min_p\{d_p\}_{p=1}^v$ should be satisfied. Following [25], μ is heuristically updated by measuring the gap of k and ι, where ι denotes the multiplicity of eigenvalue zeros. Specifically, μ is initially set to 1 and iteratively updated by $\mu = 2 \times \mu$ if $\iota \leq k$ or $\mu = \frac{\mu}{2}$ if $\iota > k+1$.

Performance is measured by accuracy (ACC), normalized mutual information (NMI), purity, and F-score [62], [63]. Experiments were performed on a desktop with Intel(R) i9 9900 K CPUs @3.6GHZ, 64 GB RAM, and Matlab 2020b.

B. Effectiveness of BGAE Compared to Baselines

Table IV reports clustering metrics, and we observe that:

1) Our novel BGAE achieves competitive performance and ranks first in most cases. Compared to the runner-up ones, ours achieves 3.31%, 4.43%, 1.98%, 6.15%, 2.50%, 3.50%, 1.44%, 4.45%, 7.74%, and 2.80% improvement of ACC on ten datasets, respectively. In particular, our superiority is evident on large-scale datasets ($n \geq 38,654$), demonstrating the effectiveness. Moreover, our end-to-end model does not require post-processing, avoiding the randomness of k-means.
2) RMKM, AMGL, FMR, and PMSC are MVC models with space complexity $\mathcal{O}(n^2)$, requiring to construct fully connected graphs, they suffer "OOM" on large-scale datasets ($n \geq 63,896$) and exhibit limited scalability, while our BGAE can still handle such challenging tasks with promising performance.
3) LMVSC and FPMVS are the two strongest MVBGC competitors. However, the separation of clustering and post-processing results in unstable performance and suboptimal solutions. Mostly, all BGC baselines only consider the "encoding" learning process but omit the "decoding" process in bipartite graph learning, their performance is inferior to ours.

C. Significance of the "encoding" Module

To reveal the discrimination of the encoded representation intuitively, Fig. 4 t-SNE visualizes the original data distribution $\{\mathbf{X}_p\}_{p=1}^v$ and the latent representation $\mathbf{V}$ on MRSCV1 (7 clusters), Dermatology (6 clusters), and ORL_3views (40 clusters). We observe that:

1) Input data stacks together and shows complex curved or folded manifold structures. The separability for disjoint clusters is inconspicuous. By contrast, by extracting the latent representation, the data show much clearer separability, even for ORL_3views that includes 40 clusters, the decision boundaries are still distinct. Although the encoded latent representation may mistake the correlation of instances caused by complex manifolds, subsequent bipartite graph learning can further exploit intrinsic structures and correct several mistaken memberships, as shown in Fig. 6.

TABLE IV
SUMMARY OF CLUSTERING METRICS

Datasets	RMKM‡	AMGL	FMR	PMSC	BMVC‡	LMVSC	SMVSC	SFMC‡	FMCNOF‡	FPMVS	SDAFG‡	Proposed‡
	ACC (%)											
Yale	61.21±0.00	64.52±4.27	*68.81±5.95*	58.80±4.43	41.21±0.00	61.47±3.47	66.06±0.00	47.27±0.00	33.94±0.00	67.27±0.00	65.45±0.00	**72.12±0.00**
3sources	49.70±0.00	20.67±0.34	59.23±5.24	*73.09±4.09*	47.34±0.00	44.26±1.90	63.63±1.29	34.91±0.00	65.09±0.00	71.01±0.00	38.46±0.00	**77.51±0.00**
MSRCV1	71.43±0.00	76.44±6.30	77.48±6.40	47.45±4.23	26.67±0.00	*83.73±7.20*	70.51±4.98	60.48±0.00	47.14±0.00	71.95±5.36	70.95±0.00	**85.71±0.00**
Dermatology	74.86±0.00	22.57±0.59	81.72±5.66	80.75±4.46	63.97±0.00	79.02±6.63	78.64±5.41	49.44±0.00	62.01±0.00	*82.96±7.44*	56.70±0.00	**89.11±0.00**
ORL_3views	55.50±0.00	71.15±2.81	65.79±3.26	63.47±3.09	48.00±0.00	65.65±2.93	65.16±1.10	50.00±0.00	27.50±0.00	66.75±0.00	*73.50±0.00*	**76.00±0.00**
ORL_4views	47.00±0.00	59.73±2.78	25.21±1.10	21.48±1.02	43.25±0.00	*61.50±2.96*	47.76±2.36	37.00±0.00	21.50±0.00	54.63±1.49	57.75±0.00	**65.00±0.00**
SUN RGB-D	19.51±0.00	9.81±0.37	OOM	OOM	21.02±0.00	17.87±0.39	*23.34±0.38*	11.02±0.00	19.67±0.00	23.26±0.50	16.85±0.00	**24.78±0.00**
YouTubeFace20	*71.10±0.00*	OOM	OOM	OOM	57.39±0.00	67.26±3.53	67.13±4.20	-	38.61±0.00	63.08±3.79	61.88±0.00	**75.55±0.00**
YouTubeFace50	OOM	OOM	OOM	OOM	66.00±0.00	68.32±2.45	*69.65±2.46*	-	21.66±0.00	64.24±2.97	62.44±0.00	**77.39±0.00**
YouTubeFace100	OOM	OOM	OOM	OOM	*70.14±0.00*	63.52±2.12	60.63±1.91	-	12.10±0.00	55.23±2.48	45.51±0.00	**72.94±0.00**
Average Rank	6.50	7.14	4.83	7.50	7.50	4.70	4.80	9.86	8.60	4.00	6.40	1.00
	NMI (%)											
Yale	64.71±0.00	67.73±1.86	**74.72±3.38**	63.74±2.98	45.58±0.00	65.43±1.92	69.83±0.00	54.27±0.00	39.50±0.00	71.06±0.00	69.20±0.00	*73.11±0.00*
3sources	35.02±0.00	8.07±0.43	45.96±2.69	**67.06±3.08**	48.86±0.00	33.13±1.89	54.35±1.62	6.28±0.00	51.96±0.00	61.72±0.00	10.37±0.00	*66.09±0.00*
MSRCV1	63.03±0.00	77.65±3.23	69.48±3.31	34.29±2.81	8.29±0.00	*78.93±4.60*	62.01±2.61	60.23±0.00	38.42±0.00	65.69±3.27	76.23±0.00	**80.50±0.00**
Dermatology	71.10±0.00	3.20±0.57	*79.97±3.67*	**85.11±1.91**	60.79±0.00	70.17±3.94	66.62±2.66	38.68±0.00	54.24±0.00	71.90±5.05	51.61±0.00	77.29±0.00
ORL_3views	76.28±0.00	87.64±1.07	81.20±1.38	80.93±1.39	69.15±0.00	83.35±1.13	84.85±0.29	81.58±0.00	49.23±0.00	86.26±0.00	**88.80±0.00**	*87.96±0.00*
ORL_4views	71.83±0.00	*80.28±1.37*	48.33±0.81	43.87±0.84	65.32±0.00	79.39±1.15	72.73±1.13	76.30±0.00	43.32±0.00	77.41±0.54	76.89±0.00	**81.13±0.00**
SUN RGB-D	**27.81±0.00**	18.46±0.66	OOM	OOM	12.98±0.00	24.50±0.37	22.71±0.41	2.30±0.00	15.66±0.00	22.84±0.82	11.37±0.00	*26.89±0.00*
YouTubeFace20	78.34±0.00	OOM	OOM	OOM	70.65±0.00	76.78±1.34	*78.36±2.39*	-	45.45±0.00	74.30±1.95	73.18±0.00	**81.17±0.00**
YouTubeFace50	OOM	OOM	OOM	OOM	81.90±0.00	82.43±0.78	*83.63±0.85*	-	43.03±0.00	82.08±1.07	77.18±0.00	**86.43±0.00**
YouTubeFace100	OOM	OOM	OOM	OOM	*82.23±0.00*	81.38±0.60	79.90±0.77	-	29.96±0.00	77.06±1.53	61.43±0.00	**84.37±0.00**
Average Rank	6.25	6.14	5.50	7.00	7.90	4.60	4.80	9.29	8.90	4.20	6.20	1.60
	Purity (%)											
Yale	62.42±0.00	66.64±3.14	*70.08±5.39*	60.47±3.92	43.03±0.00	62.40±3.27	66.06±0.00	48.48±0.00	35.15±0.00	67.27±0.00	66.06±0.00	**72.12±0.00**
3sources	59.17±0.00	21.21±0.32	67.74±2.56	78.31±2.52	67.46±0.00	60.52±1.34	75.73±1.83	35.50±0.00	66.86±0.00	*78.70±0.00*	39.05±0.00	**82.25±0.00**
MSRCV1	74.76±0.00	80.45±4.29	79.01±4.16	49.91±3.78	27.14±0.00	*85.25±5.56*	71.51±4.02	62.86±0.00	50.48±0.00	72.33±5.01	70.95±0.00	**85.71±0.00**
Dermatology	75.70±0.00	23.12±0.50	84.79±2.87	*85.37±1.89*	65.08±0.00	80.97±4.29	80.35±3.73	50.00±0.00	62.85±0.00	83.55±6.84	66.48±0.00	**89.11±0.00**
ORL_3views	61.25±0.00	76.47±2.02	69.10±2.70	67.21±2.73	51.00±0.00	69.18±2.19	72.17±1.08	**79.25±0.00**	28.25±0.00	73.75±0.00	*79.00±0.00*	78.75±0.00
ORL_4views	53.00±0.00	66.92±2.07	26.48±1.14	23.90±1.08	47.50±0.00	65.68±2.53	51.91±2.16	**78.00±0.00**	21.75±0.00	58.97±1.39	63.00±0.00	*69.50±0.00*
SUN RGB-D	**38.55±0.00**	10.74±0.37	OOM	OOM	21.13±0.00	37.42±0.53	32.64±0.65	11.47±0.00	25.15±0.00	32.77±1.15	17.65±0.00	*37.52±0.00*
YouTubeFace20	*77.24±0.00*	OOM	OOM	OOM	62.76±0.00	73.40±2.75	72.40±3.96	-	40.34±0.00	64.92±3.83	68.31±0.00	**79.45±0.00**
YouTubeFace50	OOM	OOM	OOM	OOM	*73.64±0.00*	73.21±2.18	72.72±2.61	-	22.83±0.00	66.84±3.02	67.83±0.00	**81.81±0.00**
YouTubeFace100	OOM	OOM	OOM	OOM	*74.75±0.00*	70.03±1.65	64.18±2.07	-	12.17±0.00	57.89±2.68	49.99±0.00	**75.86±0.00**
Average Rank	6.00	6.86	5.33	7.50	7.60	4.60	5.30	7.43	9.10	4.70	6.30	1.40
	F-score (%)											
Yale	42.68±0.00	41.47±3.53	*56.30±4.88*	43.23±4.15	21.15±0.00	46.42±2.74	52.60±0.00	31.28±0.00	17.97±0.00	54.19±0.00	45.91±0.00	**58.12±0.00**
3sources	44.16±0.00	26.80±0.30	56.03±4.84	**67.76±4.40**	45.93±0.00	43.64±1.98	56.95±1.14	37.77±0.00	59.00±0.00	62.81±0.00	36.74±0.00	*66.88±0.00*
MSRCV1	59.98±0.00	70.28±4.42	66.76±4.50	34.05±2.34	16.01±0.00	**77.43±6.43**	59.31±2.82	52.43±0.00	33.85±0.00	61.55±3.54	63.58±0.00	*76.42±0.00*
Dermatology	74.82±0.00	18.46±0.78	77.59±5.15	**83.50±4.24**	56.62±0.00	70.50±4.17	70.06±3.60	42.90±0.00	57.89±0.00	77.37±6.23	53.89±0.00	*82.79±0.00*
ORL_3views	41.34±0.00	53.73±6.36	54.00±3.15	52.57±3.06	31.60±0.00	56.52±3.38	55.98±0.76	32.35±0.00	13.80±0.00	*58.73±0.00*	47.51±0.00	**63.35±0.00**
ORL_4views	33.66±0.00	35.12±4.54	9.27±0.83	6.48±0.54	24.84±0.00	**50.10±2.86**	32.37±1.71	23.74±0.00	12.09±0.00	42.87±1.47	23.11±0.00	*45.96±0.00*
SUN RGB-D	13.15±0.00	6.46±0.22	OOM	OOM	15.16±0.00	11.41±0.23	14.99±0.14	12.17±0.00	14.08±0.00	*15.23±0.39*	13.80±0.00	**16.25±0.00**
YouTubeFace20	*65.59±0.00*	OOM	OOM	OOM	49.04±0.00	62.43±2.91	61.68±5.99	-	25.84±0.00	57.81±4.00	42.07±0.00	**70.40±0.00**
YouTubeFace50	OOM	OOM	OOM	OOM	57.09±0.00	62.49±2.45	*63.52±2.56*	-	15.67±0.00	56.89±3.18	24.29±0.00	**71.52±0.00**
YouTubeFace100	OOM	OOM	OOM	OOM	**59.77±0.00**	56.47±2.41	49.79±2.75	-	6.33±0.00	37.44±5.64	5.57±0.00	*59.58±0.00*
Average Rank	6.38	8.00	5.17	6.33	7.10	4.30	4.80	9.43	8.30	3.80	7.50	1.50

‡ denotes stable algorithm.
The best results are symbolized in bold, the runner-up ones are underlined and italic, "OOM" denotes out-of-memory errors, and "-" denotes time-out errors.

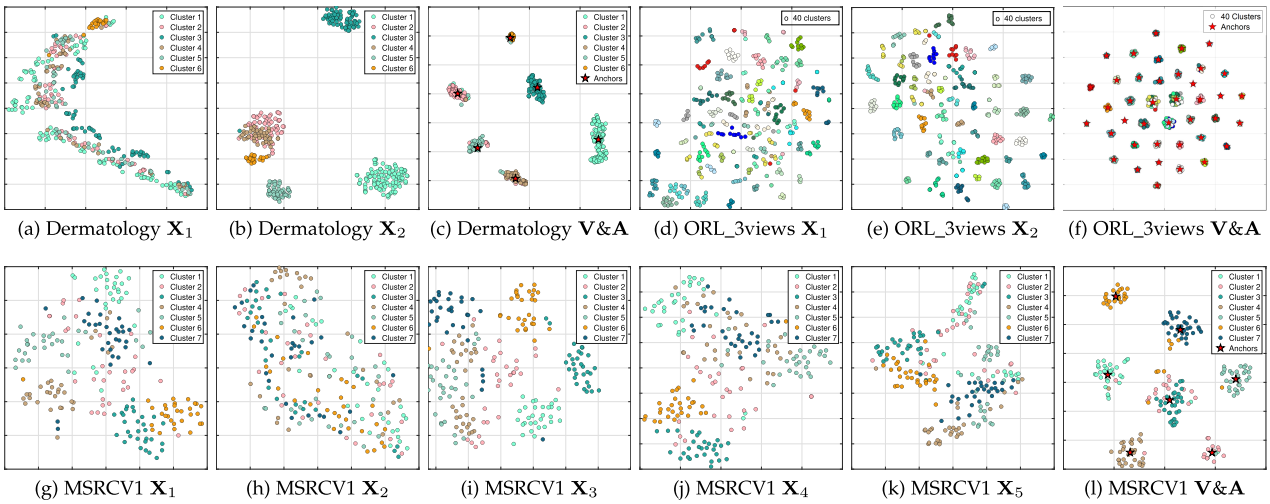

(a) Dermatology $\mathbf{X}_1$ (b) Dermatology $\mathbf{X}_2$ (c) Dermatology $\mathbf{V}\&\mathbf{A}$ (d) ORL_3views $\mathbf{X}_1$ (e) ORL_3views $\mathbf{X}_2$ (f) ORL_3views $\mathbf{V}\&\mathbf{A}$

(g) MSRCV1 $\mathbf{X}_1$ (h) MSRCV1 $\mathbf{X}_2$ (i) MSRCV1 $\mathbf{X}_3$ (j) MSRCV1 $\mathbf{X}_4$ (k) MSRCV1 $\mathbf{X}_5$ (l) MSRCV1 $\mathbf{V}\&\mathbf{A}$

Fig. 4. t-SNE visualization of the input multi-view data $\{\mathbf{X}_p\}_{p=1}^{v}$ and the extracted latent representation $\mathbf{V}$.

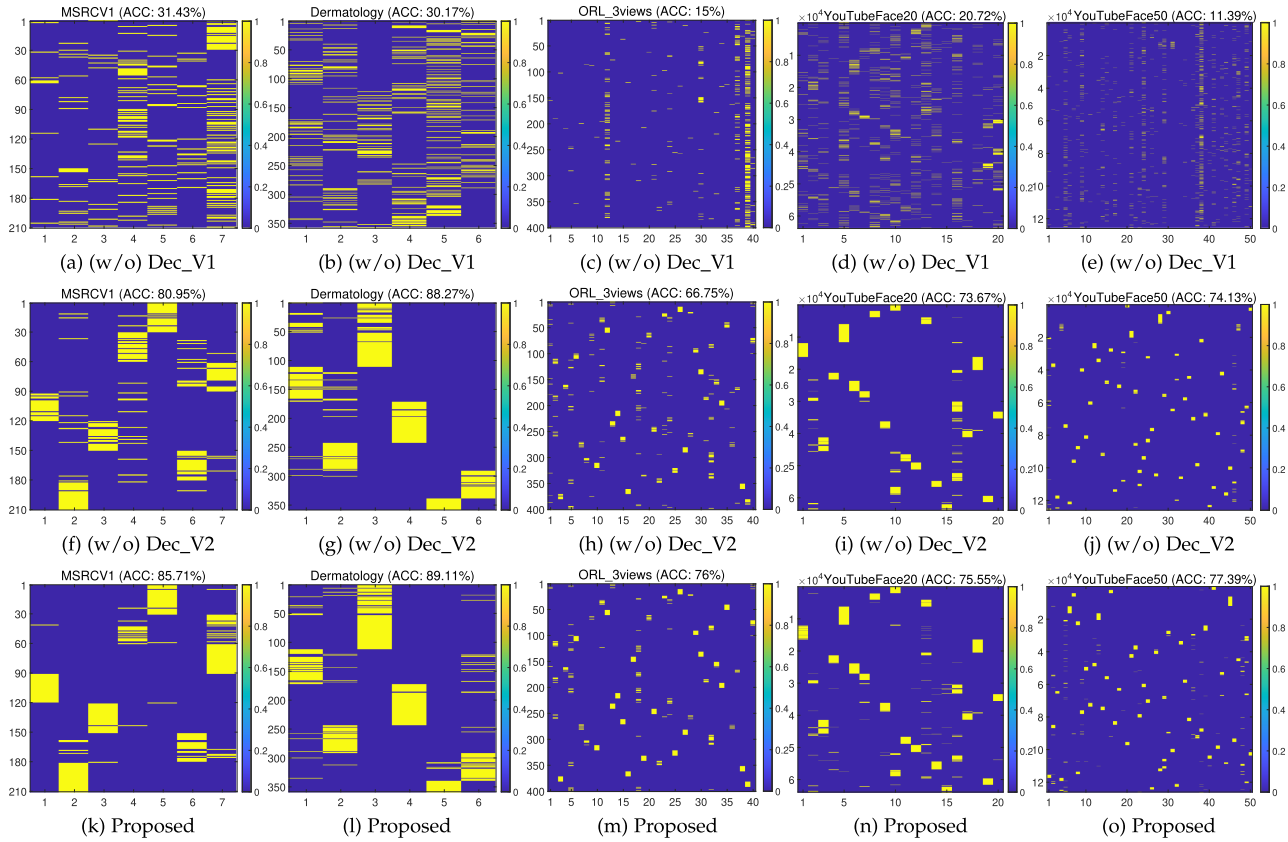

Fig. 5. Ablation analysis of the "decoding" module by visualizing the bipartite graph representation.

TABLE V
EXPERIMENTAL SETTINGS OF ABLATION ANALYSIS

Model	$\mathcal{L}_1$	$\mathcal{L}_2$	$\mathcal{L}_3$	Extra Regularizer
(w/o) Dec_V1	✓	✓	–	–
(w/o) Dec_V2	✓	✓	–	✓
Proposed	✓	✓	✓	–

2) An interesting phenomenon is that the learned anchors almost lie in the centroids of clusters, exhibiting discriminative property, and conform to our intuitive and ideal pursuit in bipartite graph learning. A reasonable explanation is that we enforce the connectivity constraint on the bipartite graph to ensure the k-connected components, making the bipartite graph $\mathbf{Z}$ sparse enough to satisfy such a constraint. Recalling anchors are optimized without constraint, and our experimental setting $m = k$ contributes to approaching the intuitive result that each anchor lies in the corresponding centroid of the cluster. The results verify the reasonability of our unconstrained optimization strategy on anchors $\mathbf{A}$.

D. Ablation Analysis of the "decoding" Module

To verify the significance of our novel "encoding-decoding" design, Table V lists ablation study settings. For simplicity, "(w/o) Dec_V1" denotes our model that removes the "decoding" module. "(w/o) Dec_V2" denotes "(w/o) Dec_V1" with a quadratic term of $\mathbf{Z}$, i.e., introducing an additional regularization term ζz_{ij}^2, where the balanced parameter ζ is heuristically pre-determined following [43]. As a reference, we also give the metrics of the latent representation $\mathbf{V}$ coupled k-means to output labels, called "LV_KM".

First, Fig. 5 visualize bipartite graphs on MSRCV1, Dermatology, ORL_3views, YouTubeFace20, and YouTubeFace50 datasets. Since we impose connectivity constraint, bipartite graphs show sparse representation. Caused by the undesirable trivial solution, "(w/o) Dec_V1" largely mistake the memberships of anchors and instances, immensely destroying graph representation. Introducing additional regularization can correct the mistaken memberships, as shown in "(w/o) Dec_V2". However, since "(w/o) Dec_V2" ignores the guidance of the "decoding" process, it still mistakes some memberships and degrades performance, as shown in MSRCV1 and ORL_3views. Mostly, the extra regularizer acts as a penalty term to avoid trivial solutions, which leads to an undesirable hyper-parameter ζ without practical interpretations, requiring additional parameter-tuning or heuristic solutions.

Furthermore, Fig. 6 quantifies clustering metrics. We observe that "(w/o) Dec_V1" outputs dramatically poor metrics. "(w/o) Dec_V2" apparently improves clustering metrics. "LV_KM" introduces unstable performance caused by the randomness of k-means. By contrast, our BGAE achieves the best metrics and outperforms baselines with large margins of 3.64%, 6.52%, 4.76%, 0.84%, 9.25%, 6.00%, 4.97%, 1.89%, 3.26%, and 3.44% of ACC, respectively. In particular, our BGAE shows significant

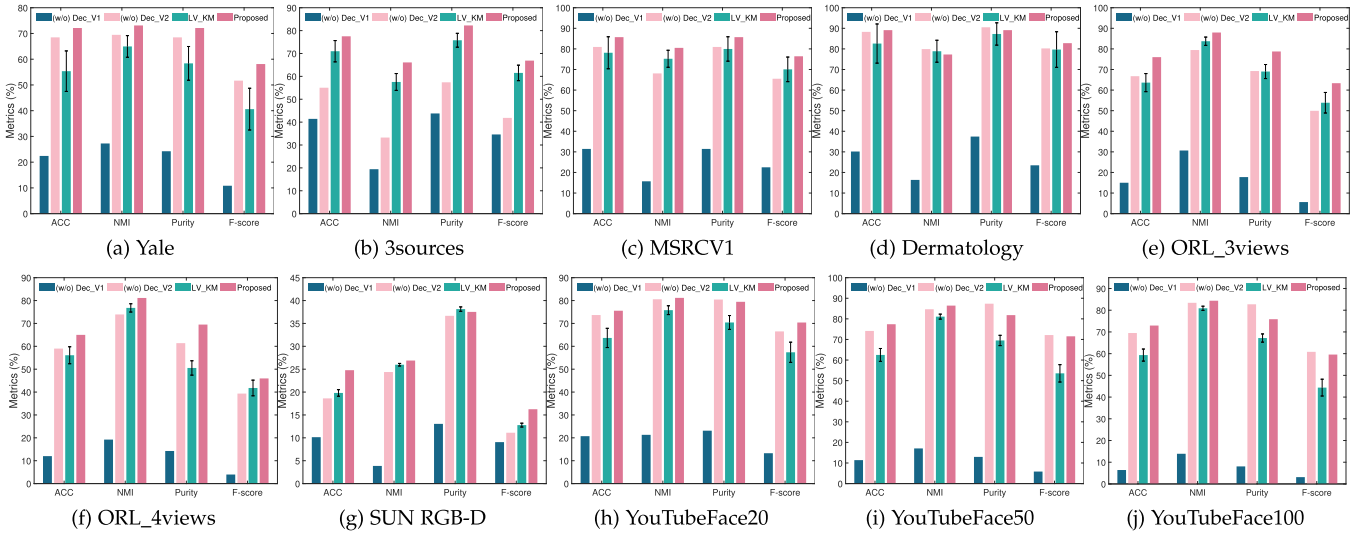

Fig. 6. Ablation analysis of the "decoding" module by quantifying the clustering metrics.

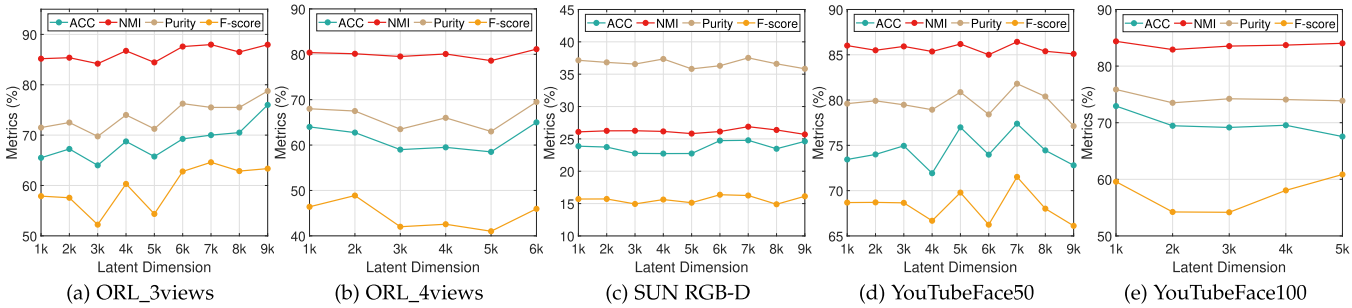

Fig. 7. Effect of latent feature dimension.

improvement over "LV_KM" in most cases, indicating that the bipartite graph construction module can further explore and refine the latent representation encoded from "encoding" module.

In summary, this is convincing evidence corroborating the effectiveness of our novel MVBGC design and the improvement brought by the "decoding" module.

E. Effect of Latent Feature Dimension

Considering pre-determining the optimal latent feature dimension d is still a challenging problem in unsupervised learning, Fig. 7 reports clustering metrics with varying latent feature dimensions in the range $[k, 2k, \ldots, 9k]$ on five datasets. As pointed in Section IV-A4, $d \leq \min_p\{d_p\}_{p=1}^{v}$ should be satisfied, the maximum latent dimension available for ORL_4views and YouTubeFace100 is $d = 6k$ and $d = 5k$, respectively. We find that dimension-metric curves show dataset-related results and do not increase monotonously but fluctuate. The results coincide with the knowledge that higher dimensions can enrich the volume of information, but may also induce redundancy or noise. How to pre-determine the optimal latent feature dimension in unsupervised learning is still an open question, which deserves future research.

F. View Weight Distribution

Fig. 8 plots the view contribution $\boldsymbol{\alpha}$ in "encoding" module. We observe that the distribution exhibits dataset-related results. Due to potential noise or redundancy within the input data, different views provide different contributions to extracting latent representation, as shown on MRSCV1, Dermatology, and ORL_3views. The results demonstrate that designing flexible and adaptive fusion mechanisms is important in multi-view learning. The $\boldsymbol{\gamma}$ distribution in the "decoding" module is available in supplementary material, available online.

G. Efficiency

Fig. 9 plots time consumption, we observe that:

1) Although our model requires comparative even more execution time compared to full graph baselines on small-scale datasets, such as Yale, 3sources, MSRCV1, and ORL_3views, which is mainly caused by complex optimization, unacceptable "OOM" on large-scale datasets

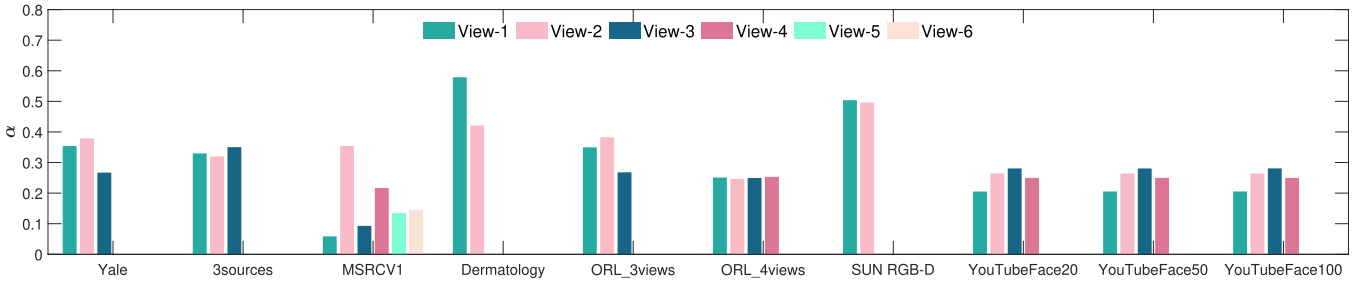

Fig. 8. View weights α in representation learning process.

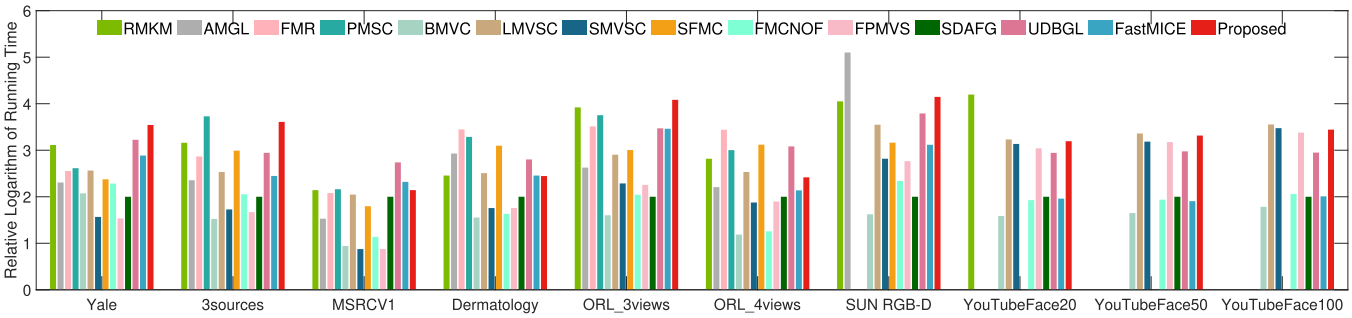

Fig. 9. Comparison of the relative logarithm running time. The compared SDAFG is the baseline.

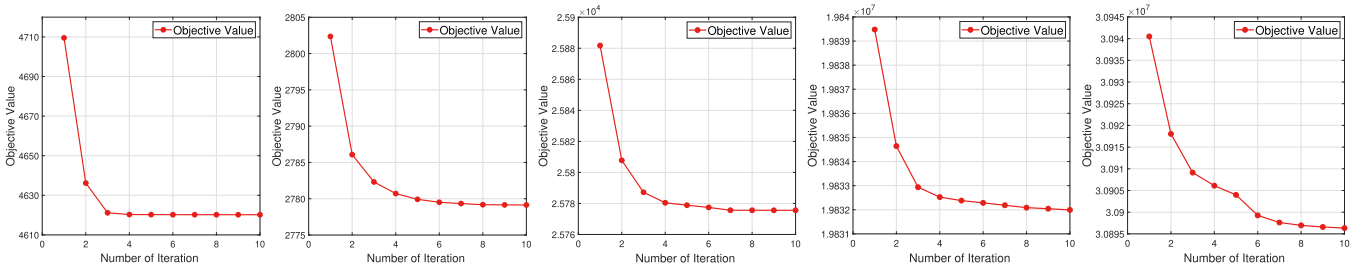

(a) MSRCV1 (b) Dermatology (c) ORL_4views (d) YouTubeFace50 (e) YouTubeFace100

Fig. 10. Empirical validation of the convergence.

will not occur for our BGAE, demonstrating the superiority of our promising scalability with linear complexity.

2) Although BGC baselines and ours share similar linear complexity, our BGAE costs comparative or more running time due to ADMM solver. However, these baselines omit the "decoding" process with degraded unstable performance. Generally, we believe that the extra computation is worthwhile for competitive performance.

H. Convergence

Our solver uses a block-coordinate descent method. The original objective in (8) is separated into eight sub-problems, and each one has a closed-form solution. Although the ALM parameter β increases iteratively, it controls the convergence speed and generally has little impact on the final results. Ideally, as β increases, the last term of (11) will be close to 0, and the ALM objective converges asymptotically to the original function bounded by 0. According to previous research on ALM framework [38], [39], the original function decreases monotonically with iterations and thus converges to a local optimal solution.

Fig. 10 empirically validates the convergence of the original function, further confirming the convergence on all benchmark datasets. Our model typically converges within 20 iterations, demonstrating its efficiency. More experimental results are provided in supplementary material, available online.

V. Conclusion

This paper revisits existing MVBGC paradigms and finds that existing models adopt a common design that encodes input data directly into bipartite graphs. Enlightened by the popular AE in deep learning, we transfer the "auto-encoding" design into traditional graph machine learning, and propose a novel BGAE

model, which consists of encoding, bipartite graph construction, and decoding modules. The encoding module extracts a latent representation from the input data in a robust manner, the bipartite graph construction module learns a discriminative bipartite graph, and the decoding module recreates the input data. All these modules are seamlessly integrated and mutually enhanced. We design an ADMM solver with linear complexity respecting instances. Empirical experiments on a synthetic dataset visualize the "benefit" of decoding learning to retain the initial manifold, and ablation analysis further verifies the effectiveness. This paper investigates how to build "auto-encoding" design in graph machine learning, we believe these novel insights will promote more variants proposed based on our novel design. This paper introduces $\ell_{2,1}$-norm to hold robustness to noise or outliers. Recent uncertainty-aware learning [64], [65] provides another solution that can measure the evidence for predictions, so developing trusted MVBGC that reduces uncertainty is meaningful. In addition, this paper assumes that the input data is complete. However, incomplete data within multi-view data is more common and challenging in real-world scenarios. So, another of our future work is to extend "auto-encoding" design to incomplete scenarios.

REFERENCES

[1] Y. LeCun, Y. Bengio, and G. Hinton, "Deep learning," *Nature*, vol. 521, no. 7553, pp. 436–444, 2015.

[2] Y. Yang et al., "Self-supervised heterogeneous graph pre-training based on structural clustering," in *Proc. Adv. Neural Inf. Process. Syst.*, New Orleans, LA, USA, 2022, pp. 16962–16974.

[3] L. Zou, F. Zhang, Y. Lin, and Y. Yu, "An efficient data structure for dynamic graph on GPUs," *IEEE Trans. Knowl. Data Eng.*, vol. 35, no. 11, pp. 11051–11066, Nov. 2023.

[4] K. Liang et al., "Knowledge graph contrastive learning based on relation-symmetrical structure," *IEEE Trans. Knowl. Data Eng.*, vol. 36, no. 1, pp. 226–238, Jan. 2024.

[5] H. Yin, A. R. Benson, J. Leskovec, and D. F. Gleich, "Local higher-order graph clustering," in *Proc. 23rd ACM SIGKDD Int. Conf. Knowl. Discov. Data Mining*, Halifax, Canada, 2017, pp. 555–564.

[6] H. Wang, Y. Yang, B. Liu, and H. Fujita, "A study of graph-based system for multi-view clustering," *Knowl. Based Syst.*, vol. 163, pp. 1009–1019, 2019.

[7] W. Zhao et al., "TelecomNet: Tag-based weakly-supervised modally cooperative hashing network for image retrieval," *IEEE Trans. Pattern Anal. Mach. Intell.*, vol. 44, no. 11, pp. 7940–7954, Nov. 2022.

[8] S. Sun, J. Fei, J. Zhao, and L. Mao, "Multi-view collaborative gaussian process dynamical systems," *J. Mach. Learn. Res.*, vol. 24, no. 258, pp. 1–32, 2023.

[9] K. Liang et al., "Reasoning over different types of knowledge graphs: Static, temporal and multi-modal," 2022, *arXiv:2212.05767*.

[10] U. Fang, M. Li, J. Li, L. Gao, T. Jia, and Y. Zhang, "A comprehensive survey on multi-view clustering," *IEEE Trans. Knowl. Data Eng.*, vol. 35, no. 12, pp. 12350–12368, Dec. 2023.

[11] S. Sun, L. Mao, Z. Dong, and L. Wu, *Multiview Machine Learning*, Berlin, Germany: Springer, 2019.

[12] S. Huang, I. W. Tsang, Z. Xu, and J. Lv, "Latent representation guided multi-view clustering," *IEEE Trans. Knowl. Data Eng.*, vol. 35, no. 7, pp. 7082–7087, Jul. 2023.

[13] H. Wang, Y. Yang, and B. Liu, "GMC: Graph-based multi-view clustering," *IEEE Trans. Knowl. Data Eng.*, vol. 32, no. 6, pp. 1116–1129, Jun. 2020.

[14] H. Xiao, Y. Chen, and X. Shi, "Knowledge graph embedding based on multi-view clustering framework," *IEEE Trans. Knowl. Data Eng.*, vol. 33, no. 2, pp. 585–596, Feb. 2021.

[15] H. Wang et al., "Debunking free fusion myth: Online multi-view anomaly detection with disentangled product-of-experts modeling," in *Proc. 31th ACM Int. Conf. Multimedia*, Ottawa, ON, Canada, 2023, pp. 3277–3286.

[16] F. Nie, W. Chang, Z. Hu, and X. Li, "Robust subspace clustering with low-rank structure constraint," *IEEE Trans. Knowl. Data Eng.*, vol. 34, no. 3, pp. 1404–1415, Mar. 2022.

[17] L. Li et al., "Local sample-weighted multiple kernel clustering with consensus discriminative graph," *IEEE Trans. Neural Netw.*, vol. 35, no. 2, pp. 1721–1734, Feb. 2024.

[18] M. Sun et al., "Scalable multi-view subspace clustering with unified anchors," in *Proc. 29th ACM Int. Conf. Multimedia*, Virtual Event, China, 2021, pp. 3528–3536.

[19] N. Zhang, X. Zhang, and S. Sun, "Efficient multiview representation learning with correntropy and anchor graph," *IEEE Trans. Knowl. Data Eng.*, to be published, doi: 10.1109/TKDE.2023.3332682.

[20] H. Zhang, F. Nie, and X. Li, "Large-scale clustering with structured optimal bipartite graph," *IEEE Trans. Pattern Anal. Mach. Intell.*, vol. 45, no. 8, pp. 9950–9963, Aug. 2023.

[21] D. Huang, C. Wang, and J. Lai, "Fast multi-view clustering via ensembles: Towards scalability, superiority, and simplicity," *IEEE Trans. Knowl. Data Eng.*, vol. 35, no. 11, pp. 11388–11402, Nov. 2023.

[22] L. Li, J. Zhang, S. Wang, X. Liu, K. Li, and K. Li, "Multi-view bipartite graph clustering with coupled noisy feature filter," *IEEE Trans. Knowl. Data Eng.*, vol. 35, no. 12, pp. 1–13, Dec. 2023.

[23] L. Li and H. He, "Bipartite graph based multi-view clustering," *IEEE Trans. Knowl. Data Eng.*, vol. 34, no. 7, pp. 3111–3125, Jul. 2022.

[24] H. Chen, F. Nie, R. Wang, and X. Li, "Fast unsupervised feature selection with bipartite graph and $\ell_{2,0}$-norm constraint," *IEEE Trans. Knowl. Data Eng.*, vol. 35, no. 5, pp. 4781–4793, May 2023.

[25] X. Li, H. Zhang, R. Wang, and F. Nie, "Multiview clustering: A scalable and parameter-free bipartite graph fusion method," *IEEE Trans. Pattern Anal. Mach. Intell.*, vol. 44, no. 1, pp. 330–344, Jan. 2022.

[26] Z. Kang, W. Zhou, Z. Zhao, J. Shao, M. Han, and Z. Xu, "Large-scale multi-view subspace clustering in linear time," in *Proc. 34th Conf. Artif. Intell.*, New York, NY, USA, 2020, pp. 4412–4419.

[27] P. Zhang et al., "Let the data choose: Flexible and diverse anchor graph fusion for scalable multi-view clustering," in *Proc. 37th AAAI Conf. Artif. Intell.*, Washington, DC, USA, 2023, pp. 11262–11269.

[28] G. E. Hinton and R. R. Salakhutdinov, "Reducing the dimensionality of data with neural networks," *Science*, vol. 313, no. 5786, pp. 504–507, 2006.

[29] P. Vincent, H. Larochelle, Y. Bengio, and P.-A. Manzagol, "Extracting and composing robust features with denoising autoencoders," in *Proc. 25th Int. Conf. Mach. Learn*, 2008, pp. 1096–1103.

[30] D. P. Kingma and M. Welling, "Auto-encoding variational bayes," 2013, *arXiv:1312.6114*.

[31] T. N. Kipf and M. Welling, "Variational graph auto-encoders," 2016, *arXiv:1611.07308*.

[32] K. He, X. Chen, S. Xie, Y. Li, P. Dollár, and R. Girshick, "Masked autoencoders are scalable vision learners," in *Proc. IEEE/CVF Conf. Comput. Vis. Pattern Recog*, 2022, pp. 16000–16009.

[33] C. Hong, J. Yu, J. Wan, D. Tao, and M. Wang, "Multimodal deep autoencoder for human pose recovery," *IEEE Trans. Image Process.*, vol. 24, no. 12, pp. 5659–5670, Dec. 2015.

[34] C. Xu, Z. Guan, W. Zhao, H. Wu, Y. Niu, and B. Ling, "Adversarial incomplete multi-view clustering," in *Proc. 28th IJCAI Int. J. Conf. Artif. Intell.*, Macao, China, 2019, pp. 3933–3939.

[35] S. Lin, W. Yang, H. Wang, Q. Tsai, and K. Li, "Stm-multifrontal QR: Streaming task mapping multifrontal QR factorization empowered by GCN," in *Proc. Int. Conf. High Perform. Comput. Netw. Storage Anal.*, St Louis, Missouri, USA, 2021, Art. no. 71.

[36] S. Lin et al., "HPS cholesky: Hierarchical parallelized supernodal cholesky with adaptive parameters," *ACM Trans. Parallel Comput.*, 2023.

[37] D. D. Lee and H. S. Seung, "Learning the parts of objects by non-negative matrix factorization," *Nature*, vol. 401, no. 6755, pp. 788–791, 1999.

[38] D. Kong, C. H. Q. Ding, and H. Huang, "Robust nonnegative matrix factorization using $\ell_{2,1}$-norm," in *Proc. 20th ACM Int. Conf. Inf. Knowl. Manag.*, Glasgow, U.K., 2011, pp. 673–682.

[39] J. Huang, F. Nie, H. Huang, and C. Ding, "Robust manifold nonnegative matrix factorization," *ACM Trans. Knowl. Discov. Data.*, vol. 8, no. 3, pp. 1–21, 2014.

[40] C. H. Q. Ding, T. Li, and M. I. Jordan, "Convex and semi-nonnegative matrix factorizations," *IEEE Trans. Pattern Anal. Mach. Intell.*, vol. 32, no. 1, pp. 45–55, Jan. 2010.

[41] C. H. Q. Ding, T. Li, W. Peng, and H. Park, "Orthogonal nonnegative matrix T-factorizations for clustering," in *Proc. 12th ACM SIGKDD Int. Conf. Knowl. Discov. Data. Mining*, Philadelphia, PA, USA, 2006, pp. 126–135.

[42] L. K. Saul and S. T. Roweis, "Think globally, fit locally: Unsupervised learning of low dimensional manifolds," *J. Mach. Learn. Res.*, vol. 4, pp. 119–155, 2003.
[43] Z. Wang, L. Zhang, R. Wang, F. Nie, and X. Li, "Semi-supervised learning via bipartite graph construction with adaptive neighbors," *IEEE Trans. Knowl. Data Eng.*, vol. 35, no. 5, pp. 5257–5268, May 2023.
[44] F. Nie, X. Dong, L. Tian, R. Wang, and X. Li, "Unsupervised feature selection with constrained $\ell_{2,0}$-norm and optimized graph," *IEEE Trans. Neural Netw. Learn. Syst.*, vol. 33, no. 4, pp. 1702–1713, Apr. 2022.
[45] X. Lu and S. Feng, "Structure diversity-induced anchor graph fusion for multi-view clustering," *ACM Trans. Knowl. Discov. Data*, vol. 17, no. 2, pp. 17:1–17:18, 2023.
[46] W. Yan, J. Xu, J. Liu, G. Yue, and C. Tang, "Bipartite graph-based discriminative feature learning for multi-view clustering, lisboa, Portugal," in *Proc. 30th ACM Int. Conf. Multimedia*, Lisboa, Portugal, 2022, pp. 3403–3411.
[47] C. H. Q. Ding, D. Zhou, X. He, and H. Zha, "R_1-PCA: Rotational invariant ℓ_1-norm principal component analysis for robust subspace factorization," in *Proc. 23th Int. Conf. Mach. Learn.*, Pittsburgh, Pennsylvania, USA, 2006, pp. 281–288.
[48] C. Xu et al., "Progressive deep multi-view comprehensive representation learning," in *Proc. 37th AAAI Conf. Artif. Intell.*, Washington, DC, USA, 2023, pp. 10557–10565.
[49] K. Fan, "On a theorem of WEYL concerning eigenvalues of linear transformations I," in *Proc. Nat. Acad. Sci. U.S.A.*, vol. 35, no. 11, pp. 652–655, 1949.
[50] X. Cai, F. Nie, and H. Huang, "Multi-view k-means clustering on Big Data," in *Proc. 23th IJCAI Int. J. Conf. Artif. Intell.*, Beijing, China, 2013, pp. 2598–2604.
[51] F. Nie, J. Li, and X. Li, "Parameter-free auto-weighted multiple graph learning: A framework for multiview clustering and semi-supervised classification," in *Proc. 25th IJCAI Int. J. Conf. Artif. Intell.*, New York, NY, USA, 2016, pp. 1881–1887.
[52] R. Li, C. Zhang, Q. Hu, P. Zhu, and Z. Wang, "Flexible multi-view representation learning for subspace clustering," in *Proc. 28th IJCAI Int. J. Conf. Artif. Intell.*, Macao, China, 2019, pp. 2916–2922.
[53] Z. Kang et al., "Partition level multiview subspace clustering," *Neural Netw.*, vol. 122, pp. 279–288, 2020.
[54] Z. Zhang, L. Liu, F. Shen, H. T. Shen, and L. Shao, "Binary multi-view clustering," *IEEE Trans. Pattern Anal. Mach. Intell.*, vol. 41, no. 7, pp. 1774–1782, Jul. 2019.
[55] B. Yang, X. Zhang, F. Nie, F. Wang, W. Yu, and R. Wang, "Fast multi-view clustering via nonnegative and orthogonal factorization," *IEEE Trans. Image Process.*, vol. 30, pp. 2575–2586, 2020.
[56] S. Wang et al., "Fast parameter-free multi-view subspace clustering with consensus anchor guidance," *IEEE Trans. Image Process.*, vol. 31, pp. 556–568, 2022.
[57] S. Fang, D. Huang, X. Cai, C. Wang, C. He, and Y. Tang, "Efficient multi-view clustering via unified and discrete bipartite graph learning," *IEEE Trans. Neural Netw.*, to be published, doi: 10.1109/TNNLS.2023.3261460.
[58] J. M. Winn and N. Jojic, "LOCUS: Learning object classes with unsupervised segmentation," in *Proc. IEEE 10th Int. Conf. Comput. Vis.*, Beijing, China, 2005, pp. 756–763.
[59] X. Li, Y. Sun, Q. Sun, and Z. Ren, "Consensus cluster center guided latent multi-kernel clustering," *IEEE Trans. Circuits Syst. Video Technol.*, vol. 33, no. 6, pp. 2864–2876, Jun. 2023.
[60] X. Zhang, Y. Yang, D. Zhai, T. Li, J. Chu, and H. Wang, "Local2global: Unsupervised multi-view deep graph representation learning with nearest neighbor constraint," *Knowl. Based Syst.*, vol. 231, 2021, Art. no. 107439.
[61] Y. Liu et al., "Dink-Net: Neural clustering on large graphs," in *Proc. 40th Int. Conf. Mach. Learn.*, Honolulu, Hawaii, USA, 2023, pp. 21794–21812.
[62] S. Sun, W. Dong, and Q. Liu, "Multi-view representation learning with deep gaussian processes," *IEEE Trans. Pattern Anal. Mach. Intell.*, vol. 43, no. 12, pp. 4453–4468, Dec. 2021.
[63] X. Li, Q. Sun, Z. Ren, and Y. Sun, "Dynamic incomplete multi-view imputing and clustering," in *Proc. 30th ACM Int. Conf. Multimedia*, Lisboa, Portugal, 2022, pp. 3412–3420.
[64] M. Sensoy, L. M. Kaplan, and M. Kandemir, "Evidential deep learning to quantify classification uncertainty," in *Proc. Adv. Neural Inf. Process. Syst.*, Montréal, Canada, 2018, pp. 3183–3193.
[65] C. Xu, W. Zhao, J. Zhao, Z. Guan, X. Song, and J. Li, "Uncertainty-aware multiview deep learning for Internet of Things applications," *IEEE Trans. Ind. Inform.*, vol. 19, no. 2, pp. 1456–1466, Feb. 2023.

Liang Li received the bachelor's degree from Huazhong University of Science and Technology (HUST), Wuhan, China, in 2018, and the master's degree from the National University of Defense Technology (NUDT), Changsha, China, in 2020. He is currently working toward the PhD degree since 2021. Now, he is a visiting PhD student with A*STAR Centre for Frontier AI Research, Singapore. His research interests include graph learning and self-supervised learning.

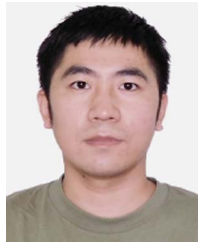

Yuangang Pan received the PhD degree in computer science from the University of Technology Sydney (UTS), Ultimo, NSW, Australia, in 2020. He is working as a research scientist with the A*STAR Centre for Frontier AI Research, Singapore. He has authored or coauthored articles in various top journals, such as *Journal of Machine Learning Research*, *IEEE Transactions on Pattern Analysis and Machine Intelligence*, *IEEE Transactions on Neural Networks and Learning Systems*, *IEEE Transactions on Knowledge and Data Engineering*, and *ACM Transactions on Information Systems*. His research interests include deep clustering, deep generative learning, and robust ranking aggregation.

Jie Liu received the PhD degrees in computer science from the National University of Defense Technology (NUDT), Changsha, China. He is a professor with the College of Computer, National University of Defense Technology. His research interests include high performance computing and machine learning.

Yue Liu received the bachelor's degree from the Northeastern University, Qinhuangdao, China, in 2021. He is currently working toward the master degree with the National University of Defense Technology, Changsha, China. His current research interests include graph neural networks, deep clustering and self-supervised learning.

Xinwang Liu (Senior Member, IEEE) received the PhD degree from the National University of Defense Technology (NUDT), Changsha, China, in 2013. He is currently a full professor with the School of Computer, NUDT. His current research interests include kernel learning and unsupervised feature learning. He has published more than 100 peer-reviewed papers, such as *IEEE Transactions on Pattern Analysis and Machine Intelligence*, *IEEE Transactions on Knowledge and Data Engineering*, *IEEE Transactions on Image Processing*, *IEEE Transactions on Neural Networks and Learning Systems*, *IEEE Transactions on Multimedia*, *IEEE Transactions on Information Forensics and Security*, ICML, NeurIPS, ICCV, CVPR, AAAI, and IJCAI. He serves as an associated editor of the TNNLS and TCYB.

Kenli Li (Senior Member, IEEE) received the PhD degree from the Huazhong University of Science and Technology (HUST), China, in 2003. He is currently a full professor of computer science and technology with Hunan University and director of the National Supercomputing Center, in Changsha. His research interests include parallel and distributed computing, high-performance computing, AI, cloud computing, and Big Data. He has published more than 600 research papers, such as *IEEE Transactions on Computers*, *IEEE Transactions on Parallel and Distributed Systems*, *IEEE Transactions on Cloud Computing*, *IEEE Transactions on Knowledge and Data Engineering*, DAC, AAAI, ICPP, etc. He serves as the editorial board of TC.

Ivor W. Tsang (Fellow, IEEE) is the director of A*STAR Centre for Frontier AI Research, Singapore. He is a professor of artificial intelligence with the University of Technology Sydney (UTS), Australia, and the research director of the Australian Artificial Intelligence Institute (AAII). His research interests include transfer learning, deep generative models, learning with weakly supervision, Big Data analytics for data with extremely high dimensions in features, samples and labels. He was the recipient of the ARC Future Fellowship for his outstanding research on Big Data analytics and large-scale machine learning, in 2013. In 2019, his JMLR article toward ultrahigh dimensional feature selection for Big Data was the recipient of the International Consortium of Chinese Mathematicians Best Paper Award. In 2020, he was recognized as the AI 2000 AAAI/IJCAI Most Influential Scholar in Australia for his outstanding contributions to the field between 2009 and 2019. He serves as the Editorial Board for JMLR, MLJ, JAIR, TPAMI, TAI, TBD, and TETCI. He serves/served as an AC or Senior AC for NeurIPS, ICML, AAAI, and IJCAI, and the steering committee of ACML.

Keqin Li (Fellow, IEEE) received the BS degree in computer science from Tsinghua University, in 1985 and the PhD degree in computer science from the University of Houston, in 1990. He is currently a SUNY Distinguished professor with the State University of New York and a National Distinguished Professor with Hunan University (China). He has authored or co-authored more than 950 journal articles, book chapters, and refereed conference papers. He received several best paper awards from international conferences including PDPTA-1996, NAECON-1997, IPDPS-2000, ISPA-2016, NPC-2019, ISPA-2019, and CPSCom-2022. He holds nearly 70 patents announced or authorized by the Chinese National Intellectual Property Administration. He is among the world's top five most influential scientists in parallel and distributed computing in terms of single-year and career-long impacts based on a composite indicator of the Scopus citation database. He was a 2017 recipient of the Albert Nelson Marquis Lifetime Achievement Award. He received the Distinguished Alumnus Award from the Computer Science Department with the University of Houston, in 2018. He received the IEEE TCCLD Research Impact Award from the IEEE CS Technical Committee on Cloud Computing, in 2022 and the IEEE TCSVC Research Innovation Award from the IEEE CS Technical Community on Services Computing, in 2023. He is a member of the SUNY Distinguished Academy. He is an AAAS fellow, an IEEE fellow, and an AAIA fellow. He is a Member of Academia Europaea (Academician of the Academy of Europe).